國立臺灣大學工學院應用力學研究所

博士論文

Graduate Institute of Applied Mechanics

College of Engineering

National Taiwan University

Doctoral Dissertation

晶圓級薄膜機械性質萃取技術之研發

CMOS-MEMS Testkey for Wafer-Level Mechanical Properties Extracting

莊婉君

Wan-Chun Chuang

指導教授：張培仁 博士

胡毓忠 博士

Advisor: Pei-Zen Chang, Ph.D.

Yuh-Chung Hu, Ph.D.

中華民國 100 年 7 月

July, 2011

謝誌

這份論文的完成要感謝許多人的幫助。首先我要感謝我的家人，感謝我的父母多年來對我的付出與栽培，並給予我最大的支持與鼓勵，讓我有即使遭遇再大的挫折也能努力走下去的勇氣，也感謝姊姊在我求學的階段裡，一肩擔起家中的開銷，讓我可以無後顧之憂的繼續求學。謝謝我的家人給我最大的支持與最溫暖的關愛，你們是我的最大精神支柱。

研究的路上，感謝 張培仁教授的指導，張老師為人幽默且博學多聞，在與老師的談話過程中，常常能得到許多建設性的啟發，張老師對於許多問題的見解十分精闢，總是讓我時時感受到老師的思慮周密，使得學生受益良多。此外，特別感謝宜蘭大學 胡毓忠老師在研究上對學生不厭其煩的用心指導，並且引領學生往正確的方向前進，且於論文撰寫期間耐心校核，讓本文得以順利完成，在此由衷感謝胡老師的指導與提攜。

感謝口試委員 黃榮堂老師、 方維倫老師、 楊龍杰老師、 戴慶良老師、 施文彬老師與台積電 林宗賢副理，對本文細心縝密的指正與提供建議，使論文結構更為嚴謹，內容更臻完善，在此表示最誠摯的感謝。

在研究生活之中，特別感謝台積電家驊學長與工研院建銘哥給予許多製程與結構設計上的建議，奕傑學長指導 layout 設計與後製程的實驗，台大貴儀中心 紀素貞小姐幫忙拍攝出十分漂亮的 SEM 照片，與實驗室的眾多學長與學弟們 小祥、小金、關恕、育諺、宣又、仁傑、小丁、家緯、怡宏、柏霖、昶文、郁智、峻安、海鄰、文章、小江、小 bee、建君在研究上的幫助在各方面互相切磋、互相合作、互相協助，美芳協助處理實驗室各項事務，六年來的時光需要感謝的人太多，感謝曾經幫助我提攜我的各位。

最後，僅以本文獻給我的家人，及所有關心鼓勵我的朋友們，一起分享這份喜悅，謝謝大家！

莊婉君 2011/8/9 謹誌於台大

中文摘要

本研究研發出一套適用於晶圓級檢測(wafer level testing)的材料機械性質量測技術。研究中發展一套以電信號與白光干涉儀(White Light Interferometers)檢測結果，萃取薄膜材料性質的演算法。本研究先以尤拉樑(Euler's beam)模型以及最小能量法(minimum energy method)為理論基礎，推導出具初始應力之微橋狀樑在承受靜電負載下的吸附電壓(pull-in voltage)的近似解析解(approximate analytical solution)，藉由量測兩組長度不同的橋狀樑測試鍵(bridge-type testkey)之吸附電壓，反算其楊氏模數(Young's modulus)與平均應力(mean stress)；再利用樑之撓曲公式(flexure formula)與彈性曲線方程式(elastic curve)，藉由量測懸臂樑型測試鍵(cantilever-type testkey)因應力釋放之自由端最大變形量，進而求得梯度應力(gradient stress)。研究中以台積電 0.18 微米製程之 metal 2 作為測試結構材料，及參考 Osterberg 發表之文獻中提供的(100)單晶矽橋狀樑、(110)單晶矽橋狀樑之吸附電壓實驗值，使用本研究提出的演算法進行材料參數萃取，所得之楊氏模數、平均應力與梯度應力數值均具有良好的準確度。此外，本研究並探討此演算法之穩健性(robustness)影響因素包含吸附電壓量測之靈敏性分析(sensitivity analysis)與測試鍵尺寸效應(dimension effects)，以提供元件設計者作為設計參考指標。本研究建立之晶圓級薄膜機械性質萃取技術，可利用現有之半導體製程中使用的量測設備，於晶圓製程線上進行量測與監控。

關鍵字：楊氏模數、平均應力、梯度應力、積體電路相容之微機電技術。

Abstract

This research develops the technologies of mechanical characterization of CMOS-MEMS devices, and presents a robust algorithm for extracting mechanical properties, such as Young's modulus, mean stress, and gradient stress, through the external electrical circuit behavior and pre-deformation of the micro test-key. First, an approximate analytical solution for the pull-in voltages of bridge-type testkey subjected to electrostatic loads and initial stress is derived based on the Euler's beam model and the minimum energy method. Then one can use the aforesaid closed form solution of the pull-in voltage to extract the Young's modulus and mean stress of the test structures. Second, according to the flexure formula and elastic curve of a cantilever beam, the gradient stress can be obtained by measuring the pre-deformation of the cantilever-type testkey utilizing White Light Interferometer. The test cases include the testkeys fabricated by TSMC 0.18 μm standard CMOS process, and the experimental results refer to Osterberg's work about the pull-in voltage of single crystal silicone micro bridges. The extracting material properties calculated by the present algorithm are valid. Besides, this research study the robustness of this algorithm including sensitivity analysis for pull-in voltage measurement and dimension effects of testkeys. This mechanical properties extracting method is expected to be applicable to the wafer-level testing in micro-device manufacture and compatible with the wafer-level testing in IC industry since the test is non-destructive.

Keyword: pull-in voltage, Young's modulus, mean stress, gradient stress, CMOS-MEMS.

Contents

謝誌..I

中文摘要 II

Abstract..III

Figures.. VI

Tables... IX

Nomenclature XI

Chapter 1 Introduction..1

1.1 State of the Art Technology 1

1.2 Thesis Structure..9

Chapter 2 Electromechanical Behavior of the Testkeys......................10

2.1 Bridge-type Testkey 10

2.1.1 Energy Expression 11

2.1.2 Approximate Analytical Solution to Pull-in Voltage.....................................13

2.2 Cantilever-type Testkey 16

Chapter 3 Wafer-Level Mechanical Properties Extracting 18

3.1 Algorithm 18

3.2 Comparison with M-TEST..21

Chapter 4 Experiment Methodology 25

4.1 Sample Preparation 25

4.2 Pull-in Voltage Detecting 30

4.2.1 Capacitance-Voltage Measurement...31

4.2.2 The Pull-in Voltage Results of Bridge-type Testkey 34

4.3 The Pre-deformation of Cantilever-type Testkey 36

4.4 Extracting Mechanical Properties of Structural Material 38

Chapter 5 Robustness Discussion 41

5.1 Sensitivity Analysis for Pull-in Voltage Measurement 41

5.2 Dimension Effects of Testkeys 44

Chapter 6 Conclusions 51

Chapter 7 Future Work 54

Publication List of the Author 55

References 56

Appendix A Capacitance-Voltage Measurement Results 60

Appendix B The Extracted Results for Common Materials 65

Figures

Figure 1 A discrete model of an equivalent spring and a parallel-plate capacitor 6

Figure 2 Nonlinear electromechanical coupling systems. 8

Figure 3 A gyroscope (a)SEM picture (b)its lumped model.......................................8

Figure 4 A microbeam resonator (a)SEM picture (b)its 1st modal shape simulated by CoventorWare. 8

Figure 5 Schematic of micro fixed-fixed beam. 11

Figure 6 Beam stress distribution. 17

Figure 7 A cantilever beam which is subjected to a bending moment at the free end. 17

Figure 8 Methodology for wafer-level mechanical properties extracting. 20

Figure 9 States of loading of a thin film for initial as-deposited or as-grown state...21

Figure 10 Scheme of the bridge-type testkey. 26

Figure 11 Scheme of the cantilever-type testkey. 26

Figure 12 Layout of the bridge-type testkey...27

Figure 13 Layout of the cantilever-type testkey. 27

Figure 14 Scheme cross-section of the bridge-type testkey, (a) after the CMOS process; (b) after post-process. 29

Figure 15 SEM picture of the bridge-type testkey after post-process. 29

Figure 16 SEM picture of the cantilever-type testkey after post-process. 30
Figure 17 The input voltage signal in the capacitance-voltage measurement. 32
Figure 18 Schematic of the experiment setup for pull-in voltage detection. 33
Figure 19 Typical sensitivities curves of the capacitances with respect to applied bias voltages of the test beam. 33
Figure 20 Capacitances-voltage curve of the bridge-type testkey with L=230 μm (V_{PI} =11.56V). 35
Figure 21 The average and standard deviation of pull-in voltage value of each test beam. 36
Figure 22 (a)Deformation curve of the cantilever-type testkey detected by WLI. (b) Shape function fitting by the commercial software Matlab. 37
Figure 23 Shape function fitting by the commercial software Matlab. 37
Figure 24 The extracted Young's modulus and mean stress of the test beams. 39
Figure 25 The measured the pull-in voltages of the fixed-fixed beams made of (100) mono-crystalline silicon in Osterberg's work. 46
Figure 26 The measured the pull-in voltages of the fixed-fixed beams made of (100) mono-crystalline silicon in Osterberg's work. 46
Figure 27 The extracted Young's modulus and mean stress of the test test beams made of (100) mono-crystalline silicon 47

Figure 28 The extracted Young's modulus and mean stress of the test test beams made of (110) mono-crystalline silicon. 47

Figure 29 The variation of the extracted values by this work. 48

Figure 30 Testkeys design in the different divisions in the same △L condition. 50

Figure 31 Testkeys set at the dicing path...53

Tables

Table 1 Summary of actuation and measurement methods for extracting material properties. 4
Table 2 Geometrical parameters of the mono-crystalline silicon beam samples and the measured pull-in voltages. 22
Table 3 Extracted Young's modulus and mean stress of the mono-crystalline silicon in (100) crystalline plane and the comparison with Osterberg's work............22
Table 4 Extracted Young's modulus and mean stress of the mono-crystalline silicon in (110) crystalline plane and the comparison with Osterberg's work............23
Table 5 Measurement conditions. 33
Table 6 Geometrical parameters of the bridge-type test beams................................35
Table 7 The average and standard deviation of pull-in voltage value of each test beam. 35
Table 8 Geometrical parameters of the cantilever-type test beam............................37
Table 9 The measured results of cantilever-type test beams. 38
Table 10 Extracted Young's modulus and mean stress of structural material fabricated by TSMC 0.18 μm 1P6M standard CMOS process...................................39
Table 11 Extracted gradient stress of structural material fabricated by TSMC 0.18 μm 1P6M standard CMOS process. 40

Table 12 The variations of the extracted Young's modulus and mean stress. 44

Table 13 The extracted results for material made by mono-crystalline silicon (△L= 50 μm). 49

Table 14 The extracted results for common structural materials. 52

Nomenclature

Symbol	Description
A	The overlapping area of upper electrode and bottom electrode
b	Width of the test structure
C	Capacitance
E	Young's modulus
g	Gap between upper electrode and bottom electrode
h	Thickness of the test structure
I	The area moment of inertia
L	Length of the test structure
U_e	Electrical potential energy
U_m	Mechanical strain energy
U	Total potential energy of the system
V	DC bias
Vs	AC testing signal
w	The deflection function
ε	The permittivity of the dielectric between beam and ground
η	The associated modal participation factor

$\widetilde{E}$	Young's modulus
$\Delta\widetilde{E}$	The corresponding variations of extracted Young's modulus
σ_0	Mean stress
$\Delta\widetilde{\sigma}_0$	The corresponding variations of extracted mean stress
σ_1	Gradient stress
$\Delta\widetilde{\sigma}_1$	The corresponding variations of extracted gradient stress
ϕ	The first natural mode of the test structure
V_{PI}	Pull-in voltage
V_{PI-ave}	The average of the measured pull-in voltage results
ΔV_{PI}	The corresponding standard deviation of measured pull-in voltage
S	The geometrical parameters of test beams
B	The geometrical parameters of test beams
ΔL	The length difference of the two test beams

Chapter 1 Introduction

Due to the well development of the technologies of complementary metal oxide semiconductor (CMOS), many micro electro mechanical systems (MEMS) devices can be fabricated by standard CMOS process, such as comb-finger [1], micro-mirror [2], and resonators [3], which are the so-called CMOS-MEMS. The main advantage of CMOS-MEMS is batch production. However, there is no standard mechanical testing for micro devices. Mechanical properties characterization of CMOS-MEMS device is important since the performance of the devices depends on the constitutive properties of the thin film made by CMOS process. It is known that the properties of thin films are different from bulk materials, depending on the deposition process. Moreover, large residual stress may induce failure of the micro devices and circuits. Therefore, the material properties, such as Young's modulus and residual stress, should be controlled as early as possible to ensure the repeatability for each device.

1.1 State of the Art Technology

The property-extraction methods for large-scale implementation in MEMS fabrication require additional measurement and actuation equipments or complicated designs of test structures. These methods are not compatible with IC metrology technologies. In the mechanical viewpoint of MEMS devices, the important thin-film

material parameters are Young’s modulus [4-15], residual stress [7, 9, 15-18], Poisson’s ratio and shear modulus [15], residual strain [8, 19], and hardness [20]. Among these mentioned parameters, Young’s modulus and residual stress have acquired the most attention. By using appropriate actuation and measurement techniques, these material properties can be extracted through determining the deformation or dynamic response of the test microstructures subjected to given external loads. Table 1 summarizes the existing techniques for extracting material properties in MEMS devices. There are six different actuation methods and six different measurement methods in Table 1. The electrostatic method employs a bias voltage to deflect the micro test structure downward to the ground plane [4-5, 8, 21]. The vibration method adopts comb driver, piezoelectric shakers, or acoustic wave to vibrate the micro test structure [6, 22]. The pulsed laser light can also be used to excite micro beams [23-24]. The force/pressure method uses the probe of atomic force microscope (AFM) or nanoindenter to apply a force on the micro test structure or apply barometric pressure on the test membrane [12-13]. The thermal method heats the test structure to deform [15]. The pre-deformation method does not need any actuation while it makes use of the deformation induced by large initial stresses [16-17, 19, 25]. Interferometer is a very common apparatus in measuring the deformation or vibration. AFM and scanning electron microscope (SEM) can also be

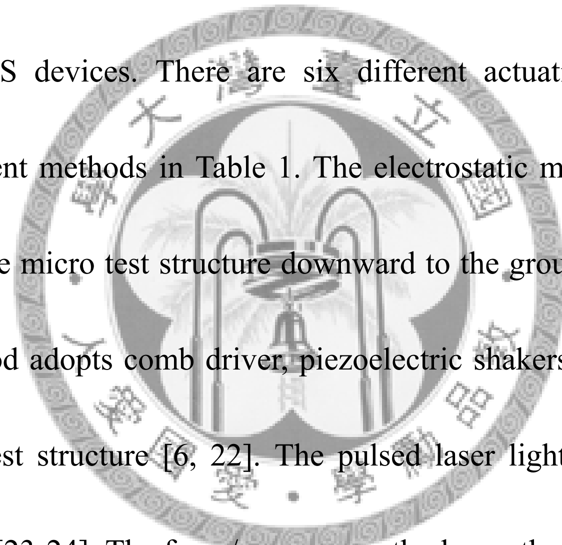

used to measure the deformation. Micro strain gauges are developed to measure the deformation [18]. Some literatures use X-Ray diffraction (XRD) to measure the indentation imprint [14, 20]. The pull-in method detects the pull-in voltage of micro test structures [9, 26-27]. Among these aforementioned techniques, the most common test structures are beams and diaphragms. Ring-type test structures have also been reported while their fundamental principals behind is very complicated and they are difficult to fabricate. Besides, nanoidenter [28] is also a common technique for extracted Young's modulus and hardness of thin films. However, this method can't extract the residual stress of thin film. The modified Stoney's equation [29] to evaluate the film stress is proposed as follows where the σ is the residual stress of thin film, $\frac{E}{(1-\nu)}$ is the biaxial modulus, h is the thickness of the substrate, t is the thickness of thin film, and R is the radius of curvature of substrate. However, this method need to the biaxial modulus of thin film first, and it is hard to deal with the case when local area with extreme variation of radius of curvature. Therefore, one can't extract the Young's modulus, mean stress, and gradient stress at the same time in each the aforesaid method.

$$\sigma = \frac{Eh^3}{6(1-\nu)Rt^2(1+\frac{t}{h})} \quad (1)$$

Table 1 Summary of actuation and measurement methods for extracting material properties.

Measuring methods	Actuating methods					
	Electrostatic	Vibration	Pulsed laser light	Force/Pressure	Thermal	Pre-deformation
Interferometer	[4-5], [8],[21]	[6], [22]	[23-24]	[7],[10]	[15]	[16-17, 19, 25]
AFM				[12-13]		
SEM				[11]		
μ strain gauge				[18]		
XRD				[14, 20]		
Pull-in	[9],[26-27]					

A viable test method must be usable at the wafer level in a manufacturing environment and, consequently, must be nondestructive. "It requires only readily available test equipment, and should be supported with documented structure-design, data-acquisition and data-analysis methods, and calibrated models for quantitative interpretation of results" [9]. Out of the known methods, the best candidate for meeting the aforementioned requirements was judged to be the use of measuring the electric-circuit behavior of the microstructures subjected to electrostatic loads.

Senturia's research group at the Massachusetts Institute of Technology (MIT) have done the important achievements about the material properties extraction of thin films through measuring the pull-in voltage of micro test structures during the past years. In 1994, Senturia [30] simulated a micro bridge-shaped beam driven by electrostatic force as a lumped model of an equivalent spring and a parallel plate

capacitor (Figure 1) in order to achieve the fundamental function forms of pull-in voltage, geometric dimension, and material parameters. Then in 1997, Senturia proposed M-Test [9] technology which showed three different micro test structures, namely, the micro-cantilever, the micro bridge-shaped beam, and the micro sector plate. Senturia also produced micro beams of different lengths to measure their pull-in voltage, respectively, in order to generalize the correcting factors based on those measured data and simulated numbers, and eventually modified the functional form based on the discrete model. However, the simpler functional form deviates far from the reality since the distributed deformation of test beams and the electromechanical coupling effects are oversimplified. Therefore, they conducted massive numerical simulations, measured a large amount of beam-type test structures with different lengths, and then obtained a more precise formula by modifying their previous functional form with many correcting factors through curve-fitting numerical simulation and measured data. The disadvantage is that the empirical formula must be used in conjunction with certain test micro structures. If the devices changes, then the formula has to change as well. Besides, the empirical formula was not easy to handle the non-ideal situations, such as the pre-deformation and non-uniform cross section of the micro test structures.

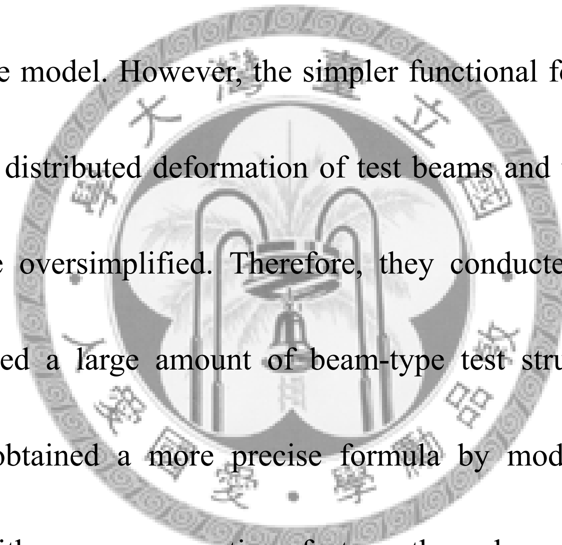

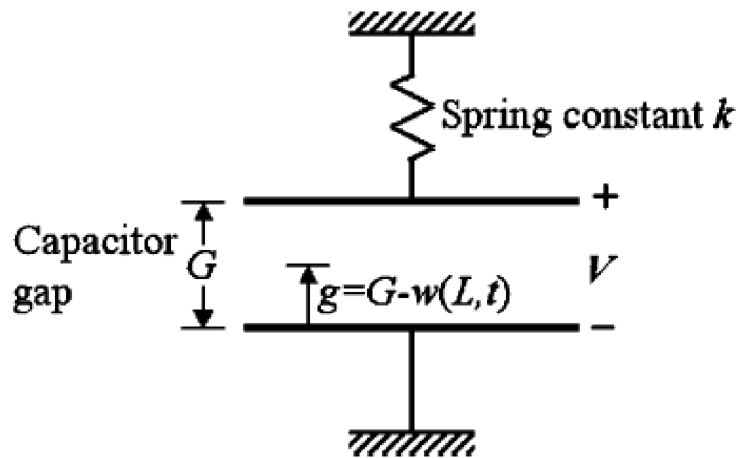

Figure 1 A discrete model of an equivalent spring and a parallel-plate capacitor [30].

The modeling of electrical-mechanical coupling behavior and the techniques of actuating and measuring are the two key technologies to the material properties extraction of thin films through measuring the electric-circuit behavior of micro test structures. A very simple lumped model was used formerly to simulate the electrostatically actuated microstructures as a parallel-plate capacitor suspended by an ideal linear spring. The lumped model has the advantage of simplicity and full analytical description but has the disadvantage of deviating far from the reality in virtue of ignoring the electrical-mechanical coupling effects, such as the non-ideal boundary conditions, fringing fields, pre-deformation due to the initial stresses, and non-homogeneous structures, as shown in Figure 2. In the past years, the study of MEMS devices mainly used numerical simulation, such as the finite element method, the boundary element method, and can simulate the actions of various structural

components with high accuracy. Its drawbacks are high computation complexity and low analysis efficiency. Therefore, related studies have explored how to reduce the large amount of computations. Hung [31] examined the methods to define grids, which are able to generate the most effective reduced model during the process of devices' working. Stewart [32] developed a set of simulation methods, which can be used for micro structures in small vibration situation. Swart [33] invented computer-aided software, named AutoMM, which can automatically produce dynamic models for micro structures. Commercial FEA/BEA tools usually used for the MEMS design, like ANSYS, ABAQUS, Maxwell, CoventorWare, CFDRC, IntelliCAD, CAEMEMS, SESES, and SOLIDIS. For example, Figure 3 shows the SEM of a micro gyroscope and its lumped model. The suspended MEMS devices can always be treated as linear lumped model under the assumption of small displacement. The whole structure can be considered as linear massless springs (flexures parts) connected to the rigid mass (the proof mass). Then, one can use the FEA tools to obtain the spring constants and the equivalent mass [34]. Besides, one can use these tools to solve the governing equations with given boundary conditions to know the mode shape of microstructures (Figure 4). Therefore, measuring the response to external loads, the material properties can be extracted through the given governing equations.

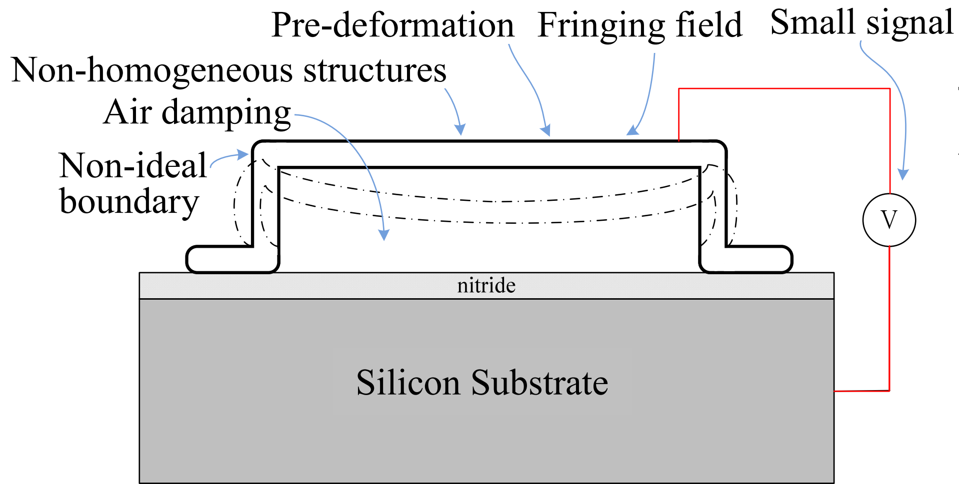

Figure 2 Nonlinear electromechanical coupling systems.

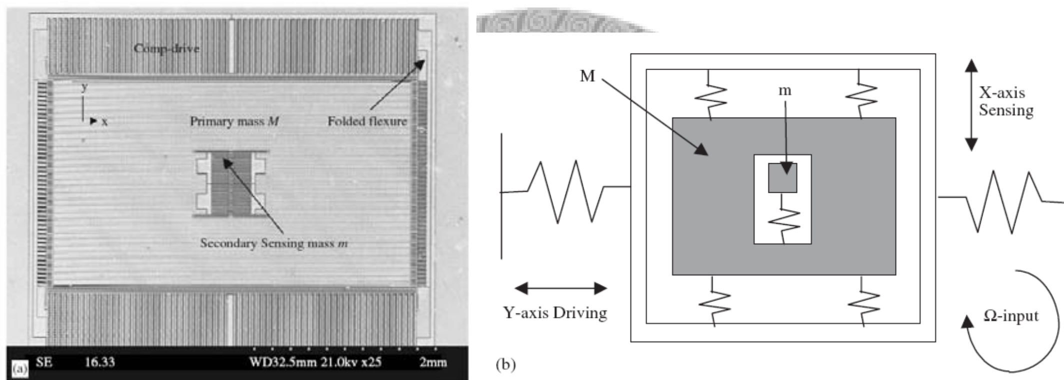

Figure 3 A gyroscope (a)SEM picture (b)its lumped model [35].

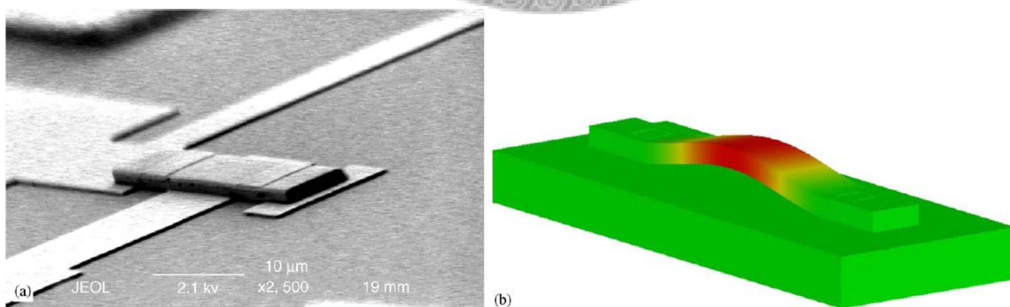

Figure 4 A microbeam resonator (a)SEM picture (b)its 1st modal shape simulated by CoventorWare [35].

Compared to the prior arts correlated with complicated or even empirical manipulation of numerical means, the objective of this research is to build simple and

valid approximate analytical models of the testkeys for extracting mechanical properties. These properties, such as Young's modulus, mean stress, and gradient stress are investigated, through the external electrical circuit behavior and pre-deformation of the micro testkeys.

1.2 Thesis Structure

In this dissertation, a robust algorithm for extracting mechanical properties, such as Young's modulus, mean stress, and gradient stress, through the external electrical circuit behavior and pre-deformation of the micro testkeys is developed. In chapter 1, motivation and background of this research with a preliminary literature survey are preformed. Chapter 2 describes in detail how electromechanical behaviors of the testkeys are derived. Chapter 3 furthermore applies the characteristic to extract mechanical properties of thin film materials. Chapter 4 reports the experiment methodology. The test beams are fabricated by TSMC 0.18 μm standard CMOS process to verify the validness of the present algorithm. Moreover, chapter 5 reveals robustness discussion including sensitivity analysis for pull-in voltage measurement and dimension effects of testkeys. The concluding section which contains some potential advantages and applications is shown in chapter 6, and chapter 7 revels the future work.

Chapter 2 Electromechanical Behavior of the Testkeys

In this chapter, the electromechanical behaviors of the testkeys are derived. Section 2.1 describes in detail about the equivalent electromechanical model of the bridge-type testkey based on the Euler’s beam model and the minimum energy method, and obtains the approximate solution of the pull-in voltage. Section 2.2 represents the equivalent model of the cantilever-type testkey according to the flexure formula and elastic curve of a cantilever beam.

2.1 Bridge-type Testkey

A conceptual diagram of a micro bridge is shown in Figure 5. The beam is of length L, width b, thickness h, and is separated from the ground by an initial gap g. As actuated by a constant drive voltage V, the electrostatic force causes a position-dependent deflection $w(x)$. The following assumptions are made to simulate the bridge.

1) The bridge is homogeneous and with uniform cross section.

2) The bridge is within the Euler-Bernoulli model.

3) Neglect the stress gradient.

4) Small deflection and ideal fixed boundary condition.

\

Figure 5 Schematic of micro fixed-fixed beam.

2.1.1 Energy Expression

The mechanical strain energy of an infinitesimal beam element is

$$dU_m = \sigma_0 \left[\frac{1}{2} \left(\frac{dw}{dx} \right)^2 \right] dv + E \left[\frac{1}{2} z^2 \left(-\frac{d^2 w}{dx^2} \right)^2 \right] dv. \tag{2}$$

The total mechanical strain energy of the beam, as shown in Figure 5, can be expressed as

$$\begin{aligned} U_m &= \int_0^L \sigma_0 \left[\frac{1}{2} \left(\frac{dw}{dx} \right)^2 \right] hb dx + \int_0^L EI \left[\frac{1}{2} \left(-\frac{d^2 w}{dx^2} \right)^2 \right] dx \\ &= \int_0^L \left[\frac{\sigma_0 bh}{2} \left(\frac{dw}{dx} \right)^2 + \frac{EI}{2} \left(\frac{d^2 w}{dx^2} \right)^2 \right] dx \end{aligned}, \tag{3}$$

where b, E, h, I, L, and w represent the beam width, Young's modulus, thickness, area inertia moment of beam cross section, beam length, and deflection, respectively. In the integrand of equation (3), the first term is the strain energy induced by initial stress (σ_0) and the second term is the bending strain energy induced by external loads. The fringing fields are considerable and must be taken into account when modeling the electrostatic loads. For an infinitesimal beam element with length dx, the differential capacitance dC is given as [36]

$$dC = \varepsilon \left[\left(\frac{b}{g-w} \right) - 1.06 + 3.31 \left(\frac{h}{g-w} \right)^{0.23} + 0.73 \left(\frac{b}{h} \right)^{0.23} \right] dx, \tag{4}$$

where ε and g represent the permittivity of dielectric medium and the initial gap

between test beam and ground plane, respectively. Hence, the total electrical potential energy U_e is given by

$$U_e = -\int_0^L \frac{1}{2}\varepsilon V^2 \left[\left(\frac{b}{g-w} \right) - 1.06 + 3.31 \left(\frac{h}{g-w} \right)^{0.23} + 0.73 \left(\frac{b}{h} \right)^{0.23} \right] dx, \qquad (5)$$

where V is the applied bias voltage. In equation (5), the first term is ideal flat plate capacitance, the second term is a length-dependent adjustment parameter, the third term is the fringing field capacitance due to beam thickness. Then, the total system energy U equals the sum of mechanical strain energy and electrical potential energy, i.e.

$$\begin{aligned} U = &\int_0^L \left[\frac{\sigma_0 bh}{2} \left(\frac{dw}{dx} \right)^2 + \frac{EI}{2} \left(\frac{d^2 w}{dx^2} \right)^2 \right] dx \\ &- \int_0^L \frac{1}{2}\varepsilon V^2 \left[\left(\frac{b}{g-w} \right) - 1.06 + 3.31 \left(\frac{h}{g-w} \right)^{0.23} + 0.73 \left(\frac{b}{h} \right)^{0.23} \right] dx \end{aligned} . \qquad (6)$$

It should be mentioned that the author is accounting for nonlinearities only in the electrostatic part of the model. Indeed, the beam structure is assumed linearly elastic, without any consideration of geometrical nonlinearity in virtue of large deformation. The author expands the electrostatic terms in equation (6) by Taylor's series with respect to the initial equilibrium position, i.e. $w = 0$, and truncate the fifth and higher order terms since $(w/g)^n \ll 1$ for n $\geqq 5$. Therefore, the total system potential energy U becomes

$$
\begin{aligned}
U = &\int_0^L \frac{\sigma_0 bh}{2}\left(\frac{dw}{dx}\right)^2 dx + \int_0^L \frac{EI}{2}\left(\frac{d^2 w}{dx^2}\right)^2 dx \\
&- \int_0^L \frac{\varepsilon V^2 b}{2g}\left(1+\left(\frac{w}{g}\right)+\left(\frac{w}{g}\right)^2+\left(\frac{w}{g}\right)^3+\left(\frac{w}{g}\right)^4\right)dx + \int_0^L \frac{1.06\varepsilon V^2}{2} dx \\
&- \int_0^L \frac{3.31\varepsilon V^2 h^{0.23}}{2g^{0.23}}\left(1+0.23\left(\frac{w}{g}\right)+\frac{0.283}{2}\left(\frac{w}{g}\right)^2+\frac{0.631}{6}\left(\frac{w}{g}\right)^3+\frac{2.038}{24}\left(\frac{w}{g}\right)^4\right)dx \\
&- \int_0^L \frac{0.73\varepsilon V^2}{2}\left(\frac{b}{h}\right)^{0.23} dx
\end{aligned}
\quad . \quad (7)
$$

2.1.2 Approximate Analytical Solution to Pull-in Voltage

The exact solution for the electrostatic-actuated beam is difficult to obtain since it is a nonlinear system with the nonlinear electrostatic force coupled with the structural deflection. Thus, such problem is often solved by the approximate analytical solution. By the use of assumed mode method [37], the deflection function $w(x)$ is expressed as

$$
w(x) = \sum_{i=1}^{n} \eta_i \phi_i(x), \quad (8)
$$

where $\phi_i(x)$ is the ith mode and the coefficient η_i to be solved is the associated modal participation factors. Then substituting the assumed deflection function into the system energy expression, one can solve for the coefficient η_i. Since the natural mode is the exact solution to the free vibration of structures, it essentially satisfies the boundary conditions and the homogeneous part of the governing equation of a dynamic system. Thus, the natural modes form the foundation for forced response calculations in structural dynamics [37]. The author adopts the first natural mode of a

fixed-fixed beam since the electrostatic loads are attractive forces and the deflection is much similar to the first natural mode of fixed-fixed beam. The first natural mode of a fixed-fixed beam is [37]

$$\phi(x) = (\cosh \lambda x - \cos \lambda x) - \zeta(\sinh \lambda x - \sin \lambda x)\,, \tag{9}$$

where the coefficients ζ and λ satisfy the following equations,

$$\zeta = \frac{\cosh(\lambda L) - \cos(\lambda L)}{\sinh(\lambda L) - \sin(\lambda L)}, \text{ and } \cos(\lambda L)\cdot\cosh(\lambda L) - 1 = 0\,. \tag{10}$$

Substituting equations (8) and (9) into equation (7) yields

$$\begin{aligned} U = {} & \int_0^L \frac{\sigma_0 bh}{2}\left(\eta\phi'\right)^2 dx + \int_0^L \frac{EI}{2}\left(\eta\phi''\right)^2 dx \\ & - \int_0^L \frac{\varepsilon V^2 b}{2g}\left(1 + \left(\frac{\eta\phi}{g}\right) + \left(\frac{\eta\phi}{g}\right)^2 + \left(\frac{\eta\phi}{g}\right)^3 + \left(\frac{\eta\phi}{g}\right)^4\right) dx + \int_0^L \frac{1.06\varepsilon V^2}{2} dx \\ & - \int_0^L \frac{3.31\varepsilon V^2 h^{0.23}}{2g^{0.23}}\left(1 + 0.23\left(\frac{\eta\phi}{g}\right) + \frac{0.283}{2}\left(\frac{\eta\phi}{g}\right)^2 + \frac{0.631}{6}\left(\frac{\eta\phi}{g}\right)^3 + \frac{2.038}{24}\left(\frac{\eta\phi}{g}\right)^4\right) dx \\ & - \int_0^L \frac{0.73\varepsilon V^2}{2}\left(\frac{b}{h}\right)^{0.23} dx \end{aligned} \quad . \tag{11}$$

The system is in static equilibrium when the first-order derivative of the total potential energy U with respect to the coefficient η equals zero, i.e. $dU/d\eta = 0$, then one have

$$\eta\left[\sigma_0 \int_0^L bh(\phi')^2 dx + E\int_0^L I(\phi'')^2 dx\right] = \frac{\varepsilon V^2}{2}\left(c_0 + c_1\eta + c_2\eta^2 + c_3\eta^3\right), \tag{12}$$

where c_j (j=0 ~3) are shown as below

$$\begin{cases} c_0 = \int_0^L \left(b/g^2 + 0.76h^{0.23}/g^{1.23} \right) \phi dx \\ c_1 = \int_0^L \left(2b/g^3 + 0.94h^{0.23}/g^{2.23} \right) \phi^2 dx \\ c_2 = \int_0^L \left(3b/g^4 + 1.04h^{0.23}/g^{3.23} \right) \phi^3 dx \\ c_3 = \int_0^L \left(4b/g^5 + 1.12h^{0.23}/g^{4.23} \right) \phi^4 dx \end{cases} . \tag{13}$$

The coefficients c_j depend only on the geometrical parameters of beam. Whether the equilibrium is stable or unstable is determined by the second-order derivative of the total potential energy with respect to η. At the transition from a stable to an unstable equilibrium, the second-order derivatives of the total potential energy with respect to η also equals zero, i.e. $d^2U/d\eta^2 = 0$, then one have

$$\left[\sigma_0 \int_0^L bh(\phi')^2 dx + E \int_0^L I(\phi'')^2 dx \right] = \frac{\varepsilon V^2}{2} \left(c_1 + 2c_2\eta + 3c_3\eta^2 \right). \tag{14}$$

Substituting equation (14) into equation (12) gives

$$2c_3\eta^3 + c_2\eta^2 - c_0 = 0. \tag{15}$$

Equation (15) is a cubic equation of η and can be solved by Cardan solution [38]. The real number root of equation (15) gives rise to the coefficient η_{PI} at pull-in as

$$\begin{aligned} \eta_{PI} = & \sqrt[3]{\left[\left(\frac{1}{4}\frac{c_0}{c_3} \right) - \left(\frac{1}{6}\frac{c_2}{c_3} \right)^3 \right] + \sqrt{\left[\left(\frac{1}{4}\frac{c_0}{c_3} \right) - \left(\frac{1}{6}\frac{c_2}{c_3} \right)^3 \right]^2 - 8\left(\frac{1}{6}\frac{c_2}{c_3} \right)^6}} \\ & + \sqrt[3]{\left[\left(\frac{1}{4}\frac{c_0}{c_3} \right) - \left(\frac{1}{6}\frac{c_2}{c_3} \right)^3 \right] - \sqrt{\left[\left(\frac{1}{4}\frac{c_0}{c_3} \right) - \left(\frac{1}{6}\frac{c_2}{c_3} \right)^3 \right]^2 - 8\left(\frac{1}{6}\frac{c_2}{c_3} \right)^6}} - \left(\frac{1}{6}\frac{c_2}{c_3} \right) \end{aligned} . \tag{16}$$

Substituting equation (16) into equation (14) gives the approximate analytical solution

to the pull-in voltage V_{PI} as

$$V_{PI}^2 = \frac{\sigma_0 \int_0^L 2bh(\phi')^2 dx + E\int_0^L 2I(\phi'')^2 dx}{\varepsilon\left(c_1 + 2c_2\eta_{PI} + 3c_3\eta_{PI}^2\right)}. \quad (17)$$

As shown in equation (17), the pull-in voltage contains two terms, the first one is dependent on initial residual stress, and the second one is dependent on beam flexibility. The pull-in voltage increases as the increasing of initial stress (σ_0) or Young's modulus (E).

A beam is considered as wide beam as $b/h \geq 5$. Wide beams exhibit plane strain conditions; therefore, the Young's modulus (E) should be replaced by the effective Young's modulus $\widetilde{E} = E/(1-\nu^2)$ and the residual stress (σ_0) should be replaced by the effective residual stress $\widetilde{\sigma}_0 = \sigma_0(1-\nu)$. Therefore, equation (17) yields

$$V_{PI}^2 = \frac{\widetilde{\sigma}_0 \int_0^L 2bh(\phi')^2 dx + \widetilde{E}\int_0^L 2I(\phi'')^2 dx}{\varepsilon\left(c_1 + 2c_2\eta_{PI} + 3c_3\eta_{PI}^2\right)}. \quad (18)$$

2.2 Cantilever-type Testkey

According to the flexure formula [39], the bending stress can be represent as

$$\sigma_x = -\frac{My}{I}, \quad (19)$$

where M is the bending moment, y is the distance from the neutral axis (up is positive), I is the moment of inertia about the neutral axis, and σ_x is bending stress which distributed in a linear manner over the cross-section. The maximum bending stress

(σ_1) is at the two outer surfaces where y is maximum. (Figure 6)

$$\sigma_1 = \frac{Mc}{I} \tag{20}$$

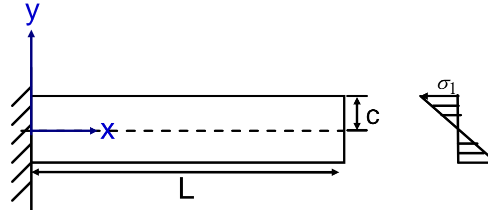

Figure 6 Beam stress distribution.

Based on the elastic curve equation (equation (21)) of a cantilever beam which is subjected to a bending moment at the free end (Figure 7), the maximum deflection can be written as equation (22) [39]

$$y(x) = \frac{Mx^2}{2EI} \tag{21}$$

$$y(L) = \frac{ML^2}{2EI} \tag{22}$$

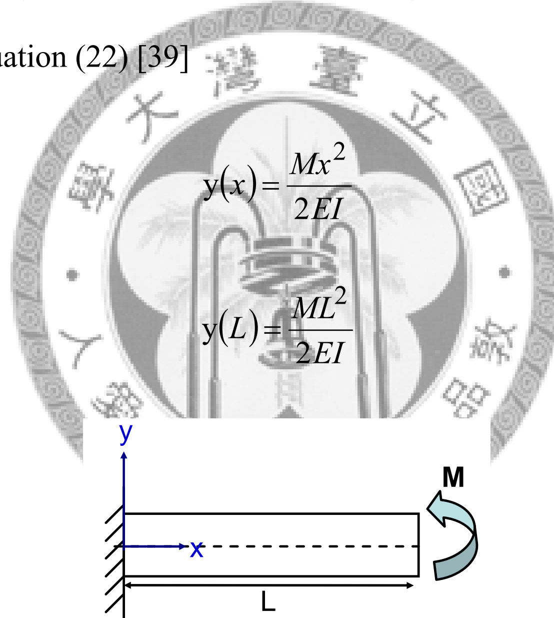

Figure 7 A cantilever beam which is subjected to a bending moment at the free end.

By equation (22) and equation (20), the stress gradient of a curled cantilever beam can be obtained as equation (23) since the maximum distance from the neutral axis (c) is equal to the half of thickness (h).

$$\sigma_1 = \frac{hEy(L)}{L^2} \tag{23}$$

Chapter 3 Wafer-Level Mechanical Properties Extracting

Chapter 2 has represented how electromechanical behaviors of the testkeys are derived. In this chapter, the author furthermore applies the characteristic of equivalent electromechanical models of the testkeys to construct an algorithm to extract mechanical properties of thin film materials. Besides, the author selects Osterberg's [9] measured data with the constant length difference $\triangle L$ of the two test beams and substituted them into the algorithm to verify the validity of the present method, and the corresponding results are shown in section 3.2.

3.1 Algorithm

The correlation between the pull-in voltage and the material parameters must be formulated quantitatively to realize the idea of extracting mechanical properties from pull-in voltage of test beam. An equilibrium equation has been derived based on Euler-Bernoulli beam model and the fringing filed capacitance model in Chapter 2. The equilibrium equation, Eq. (18) yields

$$S\tilde{\sigma}_0 + B\tilde{E} = V_{PI}^2 , \tag{24}$$

where the parameters S and B depend on the geometrical parameters of micro test beam and are given as

$$S = \frac{\int_0^L 2bh(\phi')^2\,dx}{\varepsilon\left(c_1 + 2c_2\eta_{PI} + 3c_3\eta_{PI}^2\right)}, \tag{25}$$

$$B = \frac{\int_0^L 2I(\phi'')^2 dx}{\varepsilon\left(c_1 + 2c_2\eta_{PI} + 3c_3\eta_{PI}^2\right)}. \quad (26)$$

For a given beam with the pull-in voltage V_{PI}, there are two unknowns in equation (24), i.e. $\tilde{\sigma}_0$ and $\tilde{E}$. Therefore, one needs two test beams with different length to get the two unknowns. For the two test beams made of the same material but with different length, they have the same Young's modulus and mean stress but different pull-in voltages and different S and B parameters. Then, one has two equations

$$\begin{cases} S_1\tilde{\sigma}_0 + B_1\tilde{E} = V_{PI1}^2 \\ S_2\tilde{\sigma}_0 + B_2\tilde{E} = V_{PI2}^2 \end{cases}. \quad (27)$$

By rearranging equation (24), the mean stress ($\tilde{\sigma}_0$) and Young's modulus ($\tilde{E}$) are given as the following matrix operational form,

$$\begin{Bmatrix} \tilde{\sigma}_0 \\ \tilde{E} \end{Bmatrix} = \begin{bmatrix} S_1 & B_1 \\ S_2 & B_2 \end{bmatrix}^{-1} \begin{Bmatrix} V_{PI1}^2 \\ V_{PI2}^2 \end{Bmatrix}. \quad (28)$$

One can extract Young's modulus ($\tilde{E}$) and mean stress ($\tilde{\sigma}_0$) easily by substituting the measured pull-in voltages of the two test beams with different length into equation (28). Moreover, according to the relationship between the gradient stress ($\tilde{\sigma}_1$) and maximum deflection at the free end of the cantilever-type testkey shown in equation (23), if Young's modulus ($\tilde{E}$) of structural material is given, then the gradient stress ($\tilde{\sigma}_1$) is obtained.

The methodology for wafer-level mechanical properties extracting is shown in Figure 8. First, measuring the pull-in voltages of the two bridge-type beams with

different length, then the Young's modulus ($\tilde{E}$) and mean stress ($\tilde{\sigma}_0$) will be obtained. Second, measuring the maximum deflection at the free end of the cantilever-type testkey, since the Young's modulus of structural material is obtained by the first step, the gradient stress ($\tilde{\sigma}_1$) can be known.

The residual stress ($\tilde{\sigma}_{total}$) of thin film can be represent as equation (29) [17], which is the sum of mean stress ($\tilde{\sigma}_0$) and gradient stress ($\tilde{\sigma}_1$). The scheme of states of loading of a thin film for initial as-deposited or as-grown state is shown in Figure 9 [17]. Therefore, once one knows the mean stress ($\tilde{\sigma}_0$), gradient stress ($\tilde{\sigma}_1$), and thickness h of the thin film of structural material, the variation of residual stress ($\tilde{\sigma}_{total}$) along the thickness can be obtained.

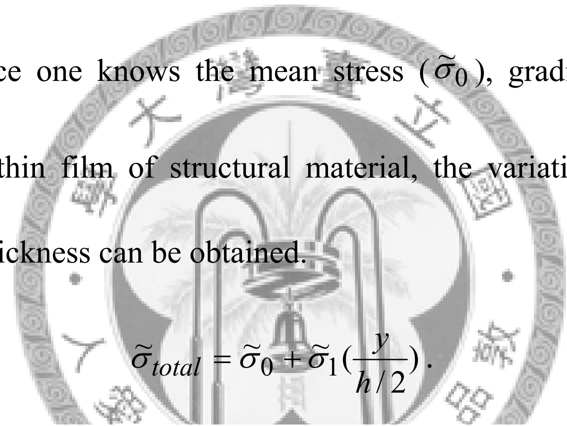

$$\tilde{\sigma}_{total} = \tilde{\sigma}_0 + \tilde{\sigma}_1 \left(\frac{y}{h/2} \right). \tag{29}$$

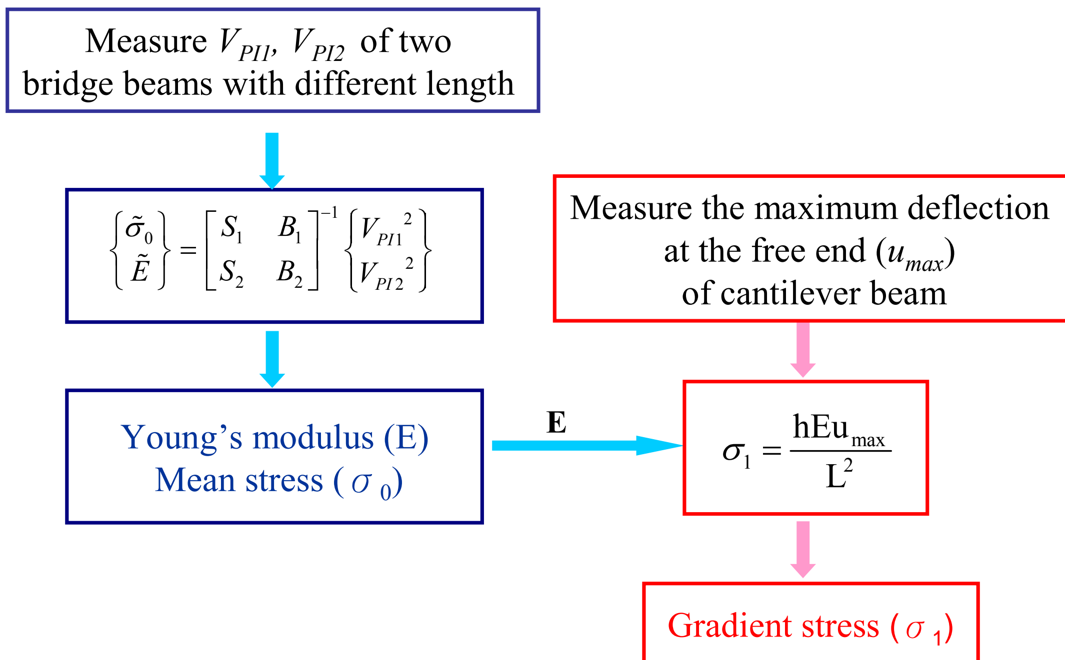

Figure 8 Methodology for wafer-level mechanical properties extracting.

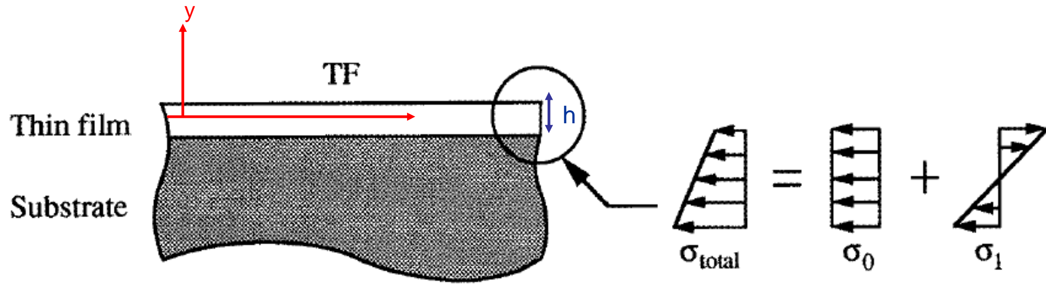

Figure 9 States of loading of a thin film for initial as-deposited or as-grown state [17].

3.2 Comparison with M-TEST

Osterberg [9] had measured pull-in voltages of numerous fixed-fixed beams with different lengths. The author selected Osterberg's measured data with the constant difference $\triangle L$ of the two test beams and substituted them into the algorithm to verify the validity of the present method.

Table 2 lists the geometrical parameters and pull-in voltages of the selected fixed-fixed beams which are made of mono-crystalline silicon. There are two groups of fixed-fixed beams listed in Table 2; each group contains six beams with different lengths. The difference of the two groups is only the crystalline plane of cross section. The first group is in the (100) crystalline plane while the second one is in the (110) crystalline plane. The author selected two beams with the constant difference $\triangle L$ from each group and substituted the measured data and beam dimensions into equation (28) to extract Young's modulus ($\widetilde{E}$) and mean stress ($\widetilde{\sigma}_0$) where $\triangle L$ is 225μm in group 1 while 275μm in group 2. Note that the cross-section of the beams

of group 1 are in the (100) crystalline plane while that of the group 2 are in the (110) crystalline plane. The Young's modulus of mono-crystalline silicon in (100) and (110) are 138 GPa and 168 GPa respectively. The mean stresses of the two beam-samples are 10 MPa [9].

Table 2 Geometrical parameters of the mono-crystalline silicon beam samples and the measured pull-in voltages [9].

Parameters	Values					
Permeability of free space ε (F/m)	8.85×10-12					
Initial gap g (μm)	1.05					
Beam width b (μm)	50					
Beam thickness h (μm)	2.94					
Length L of group 1 (ΔL=225μm)	175	400	225	450	275	500
Measured pull-in voltage V_{PI} (V)	77.38	16.9	47.79	13.78	32.65	11.56
Length L of group 2 (ΔL=275μm)	175	450	225	500	275	550
Measured pull-in voltage V_{PI} (V)	85.22	14.78	52.68	12.4	36	10.61

Table 3 Extracted Young's modulus and mean stress of the mono-crystalline silicon in (100) crystalline plane and the comparison with Osterberg's work [9].

Length difference (μm)	Length (μm)		The extracted values by this work		M-test [9]	
ΔL	L_1	L_2	E (GPa)	σ_0 (MPa)	E (GPa)	σ_0 (MPa)
225	175	400	135.35	9.97		
225	225	450	135.21	9.68	138±4	10±2
225	275	500	134.40	9.66		
Average (X_{ave})			134.99	9.77	138	10
Standard Deviation (ΔX)			0.42	0.14	4	2
$\Delta X / X_{ave}$			0.31%	1.45%	2.90%	20.00%

Table 4 Extracted Young's modulus and mean stress of the mono-crystalline silicon in (110) crystalline plane and the comparison with Osterberg's work [9].

Length Difference (μm)	Length (μm)		The extracted values by this work		M-test [9]	
ΔL	L_1	L_2	E (GPa)	σ_0 (MPa)	E (GPa)	σ_0 (MPa)
275	175	450	166.88	9.50		
275	225	500	168.16	9.53	168±6	10±1
275	275	550	167.40	9.69		
Average (X_{ave})			167.48	9.57	168	10
Standard Deviation (ΔX)			0.53	0.08	6	1
$\Delta X / X_{ave}$			0.31%	0.87%	3.57%	10.00%

Tables 3 and 4 list the extracted Young's modulus ($\widetilde{E}$) and mean stress ($\widetilde{\sigma}_0$) of mono-crystalline silicon in (100) and (110) respectively. It is shown that the extracted values of the present algorithm agree well with the average extracted value of Osterberg's results [9] but with better convergence than Osterberg's algorithm. The deviations of the extracted Young's modulus ($\widetilde{E}$) are all within 1 % which are almost tenth of the deviations of Osterberg's results [9] for both mono-crystalline silicon in (100) and (110). Besides, the deviations of the extracted mean stress ($\widetilde{\sigma}_0$) are all within 2 % which are also almost tenth of the deviations of Osterberg's results [9] for both mono-crystalline silicon in (100) and (110).

This work presents an algorithm for extracting Young's modulus ($\widetilde{E}$) and mean stress ($\widetilde{\sigma}_0$) of structural materials of MEMS devices from detecting the pull-in voltages of two micro bridge-type test beams. The author has demonstrated our method with the common structural material (mono-crystalline silicon). The extracted

values by the present method agree very well with the experimental results. The overall deviations of the extracted Young's modulus ($\widetilde{E}$) and mean stress ($\widetilde{\sigma}_0$) of the demonstrated materials are within 1% and 2%, respectively. The present algorithm is much simpler than the published work [9]. The present method is very suitable for the implementation of the mechanical characterization of capacitive MEMS devices on wafer level testing since it is non-destructive. The present algorithm can easily be written as a programming code and accompanied by an LCR meter to realize the wafer-level testing for MEMS manufacture.

Chapter 4 Experiment Methodology

Chapter 3 has constructed an algorithm of extracted mechanical properties of thin films. In this chapter, the author reports the experiment methodology, and the test beams are fabricated by TSMC 0.18 μm standard CMOS process to verify the validness of the present algorithm.

4.1 Sample Preparation

The author uses bridge-type and cantilever-type beam structures as test structures, and the scheme are shown in Figures 10 and 11 respectively. The test structures are fabricated by TSMC 0.18 μm 1P6M standard CMOS process. The upper electrode is metal 2 layer, and the bottom electrode is poly layer. The anchors are composed of metal and poly layers where via is the connecting column between each metal layer, and contact is the connecting column between metal 1 and poly layer. When a driving voltage is applied between the test structure and ground plane, the test structure will deflect downward the ground and results in capacitance variation. Figure 12 and Figure 13 reveal the layouts of bridge-type and cantilever-type testkey. There are two places which are defined as PAD layers- probing pad location and etching hole. The defined area of PAD layer at anchors is the probing pad location. It should be noticed that the probing location must keep an appropriate distance away from the test structure to avoid measurement uncertainty. The other defined area of PAD layer

between the neighboring passivation layers is etching hole which makes the sacrificial layer etched by etching solution and then results in the structure released. Since the anchors are composed of metal layer, poly layers, via and contact columns, it can reduce the under-cut effect compared to the anchors are composed of metal and poly layer without via and contact columns between that when the structures are soaked in etching solution.

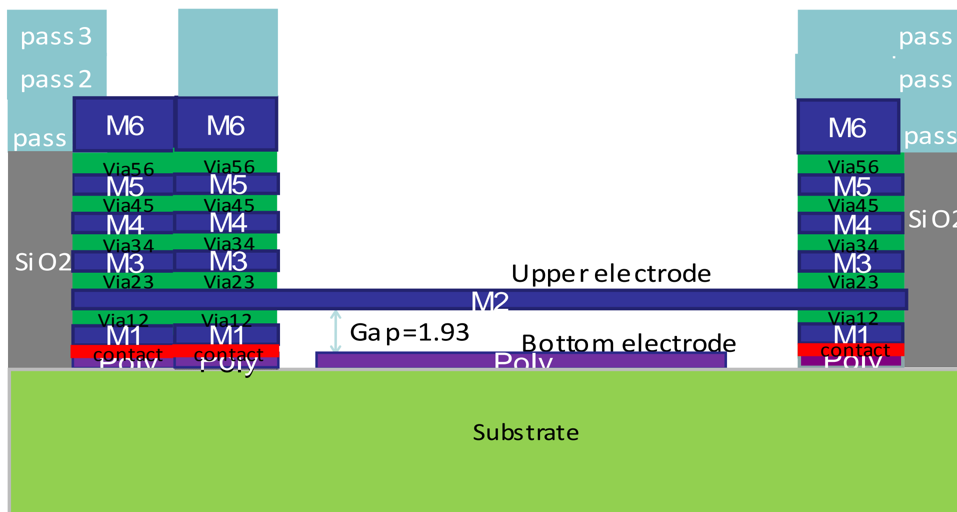

Figure 10 Scheme of the bridge-type testkey.

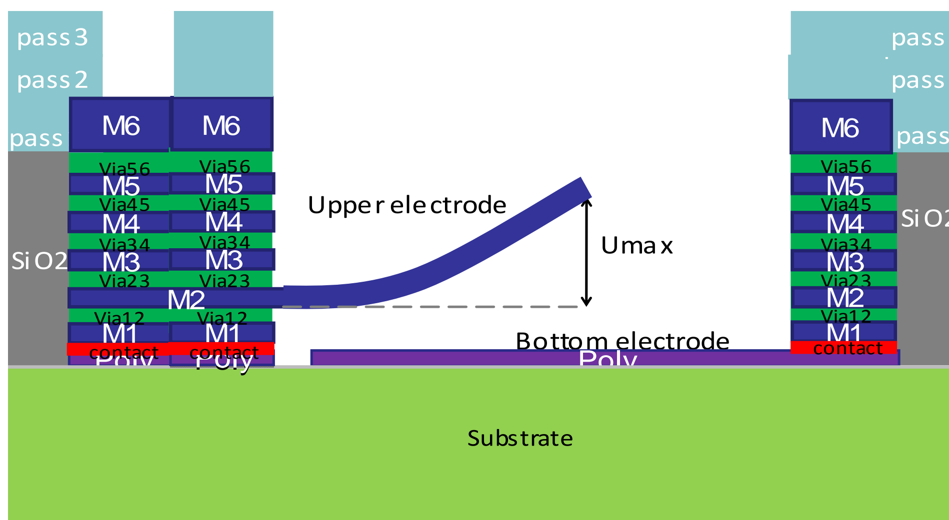

Figure 11 Scheme of the cantilever-type testkey.

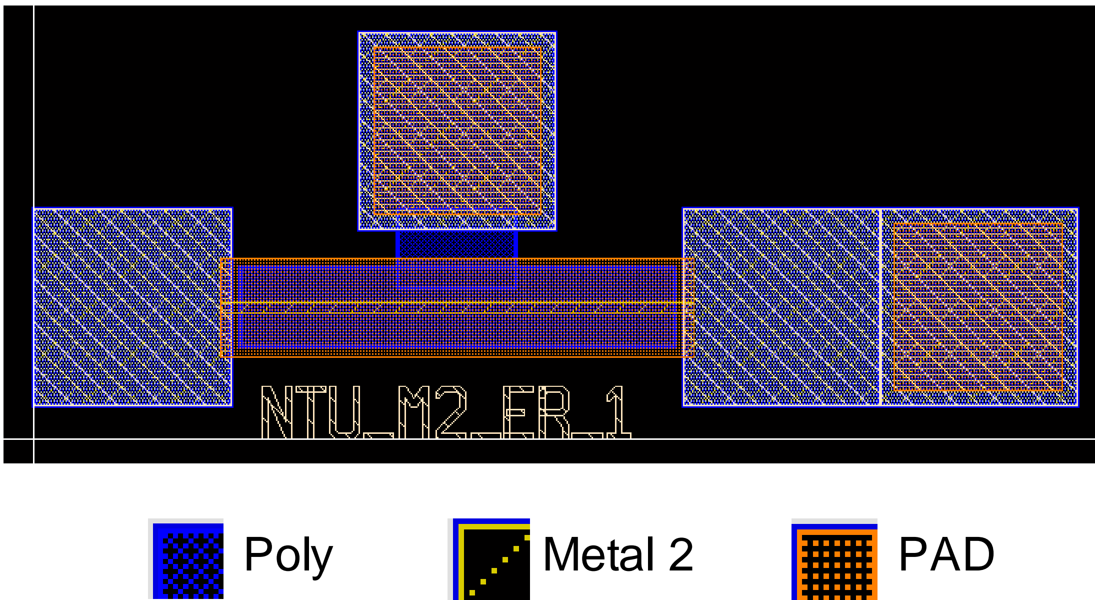

Figure 12 Layout of the bridge-type testkey.

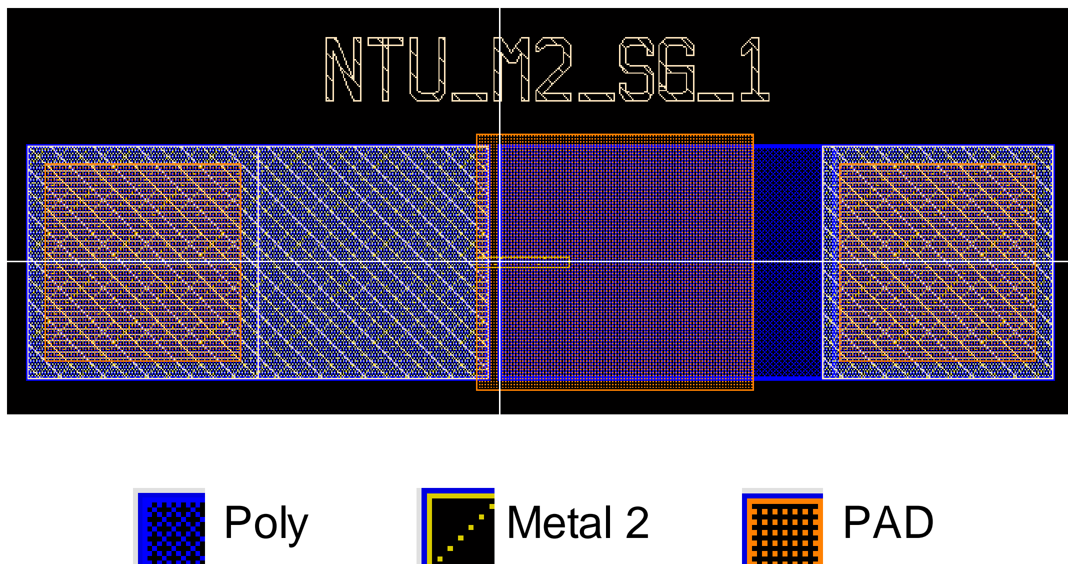

Figure 13 Layout of the cantilever-type testkey.

Figure 14 shows the schematic cross-section of the bridge-type testkey after the CMOS process and after post-process. A silicon dioxide layer between the upper electrode and the bottom electrode is a sacrificial layer (Figure 14(a)). The author

chooses Silox Vapox III as the etching solution since it has good etch rate selectivity between the metal and silicon dioxide layer. Soaking the bridge-type testkey after the CMOS process in Silox Vapox III, the etching solution will etch silicon dioxide layer through the etching hole between the neighboring passivation layers, and form a gap between both electrodes (Figure 14(b)) during post-process. Next, utilize critical point drying (CPD) method to dry the structures without collapsing to release the structures. It should be mentioned that the size of etching hole affects the released time, and the appropriate design of etching hole can make the released time shorten. Besides, setting a magnetic stirring rod below the etching solution tank can also shorten the released time, but make sure the structures has protected patterned on it to prevent the damage caused during the stirring process. Excepting the probing pad location and etching hole, the other places are covered by passivation layers to avoid the damage caused by the etching solution.

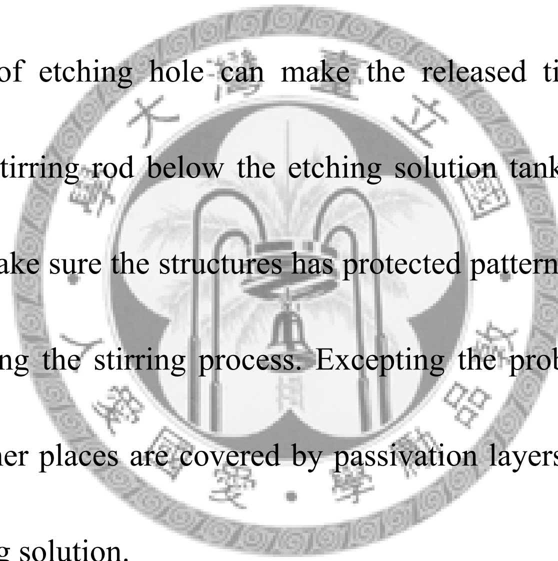

Figure 15 and Figure 16 show the SEM pictures of the bridge-type and cantilever-type testkey after post-process, and it is obvious that the testkeys are released successfully by soaking in Silox Vapox III 85 min. Furthermore, from Figure 16, one can see that the cantilever-type testkey is curled in virtue of the stress gradient.

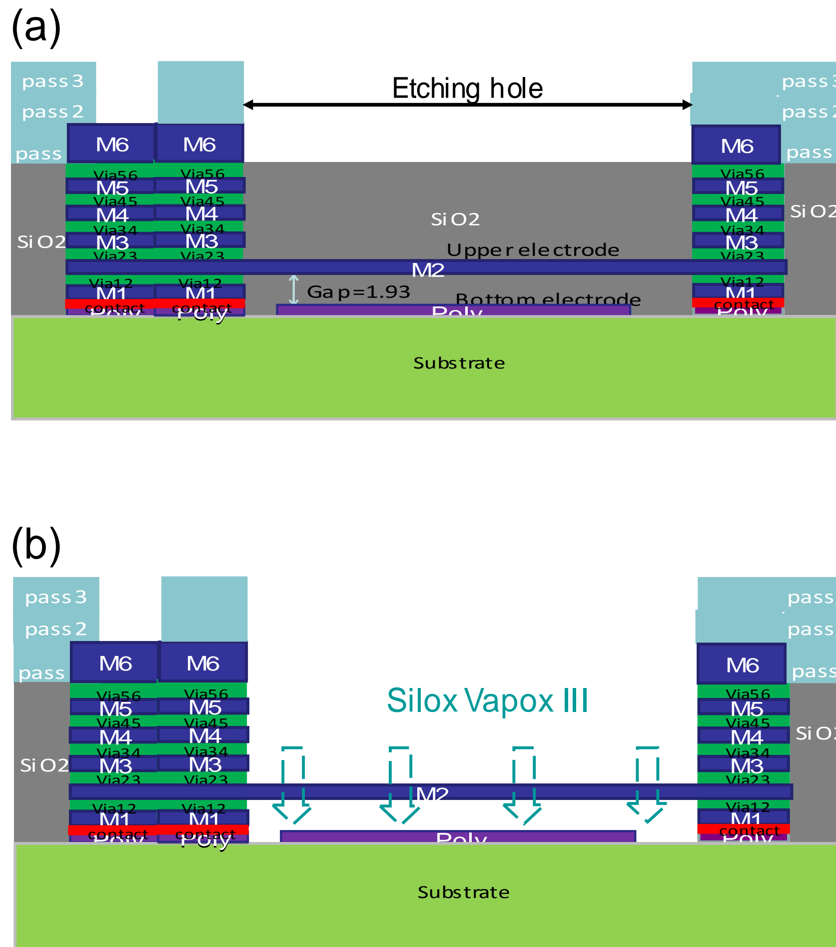

Figure 14 Scheme cross-section of the bridge-type testkey, (a) after the CMOS process; (b) after post-process.

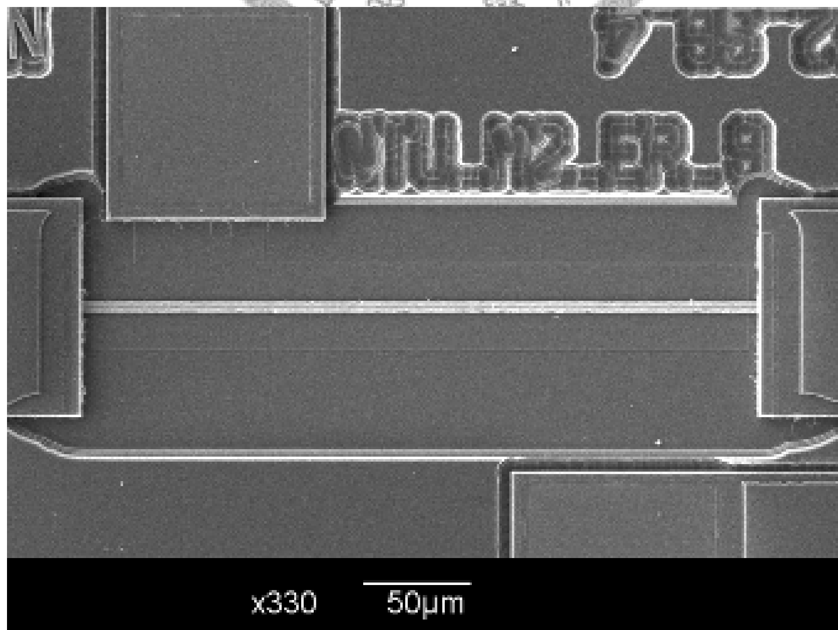

Figure 15 SEM picture of the bridge-type testkey after post-process.

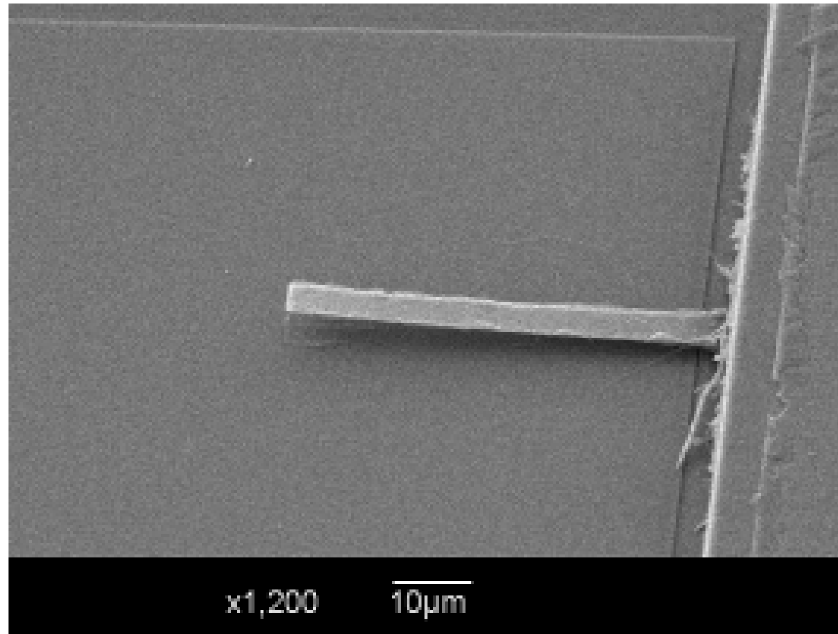

Figure 16 SEM picture of the cantilever-type testkey after post-process.

4.2 Pull-in Voltage Detecting

For a deflective microstructure subjected to electrostatic loads, as shown in Figure 5, the structural deflection causes the change of the gap between the upper and bottom electrodes and then the change of the capacitance. Therefore, the variation of capacitances to the applied bias voltages is equivalent to the deformations to the external loads, and then one can detect the pull-in voltage by tracking the capacitance sensitivities with respect to applied bias voltages. Pull-in will occur when the capacitance is with sharp increase. Through the capacitance-voltage measurement and the material property extraction algorithms mentioned in chapter 3, one can obtain the material properties of the test microstructure.

4.2.1 Capacitance-Voltage Measurement

The principle of capacitance-voltage measurement is introduced as the following. The main idea is to measure the circuit capacitive reactance X_C to yield the capacitance C. The capacitive reactance is $X_C = 1/(2\pi f C)$ where X_C, f, and C represent the circuit capacitive reactance, the testing signal frequency, and the capacitance respectively. T input driving voltage is a small AC testing signal riding on a large DC bias voltage which induces the structural deflection, as shown in Figure 17. Then the capacitance can be calculated from the circuit capacitive reactance. It should be mentioned here that the frequency of the AC testing signal must avoid the resonance frequency of the test microstructure; otherwise the capacitance will appear large fluctuation.

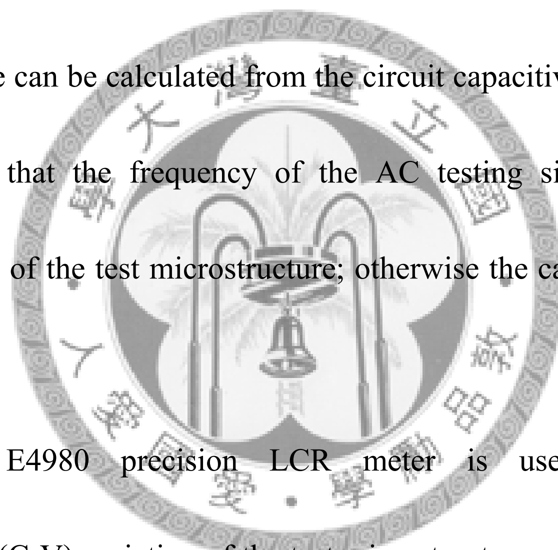

The Agilent E4980 precision LCR meter is used to measure the capacitance-voltage (C-V) variation of the test microstructure, as shown in Figure 18. The frequency and level of the AC testing signal must be set properly since they will affect the accuracy of the capacitance measurement. The author chooses the root mean square value of the test AC signal level as 25 mV and the frequency 1 MHz. The integration time is set to medium (MED). The instrument parameters setting are listed in Table 5. The author detected the pull-in voltage by tracking the capacitance sensitivities with respect to the applied bias voltages. Two low noise probes touch the

two probing pad of test beam, as shown in Figure 18. The probes are connected to the Agilent E4980 high precision LCR meter. The Agilent E4980 can supply a test signal of 25mV/1MHz riding on the bias voltages ranging from 0 to 40 V. Agilent E4980 exports the capacitance-voltage data to a personal computer and tracks the capacitance sensitivities to the applied bias voltage. Figure 19 shows the typical measured capacitance sensitivities results. Pull-in will occur when the capacitance is with sharp increase. Therefore, according to the results from capacitance-voltage measurement, one can obtain the pull-in voltage of the test beam exactly.

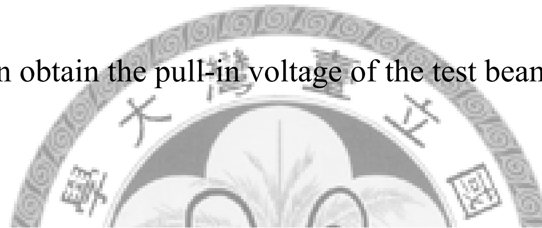

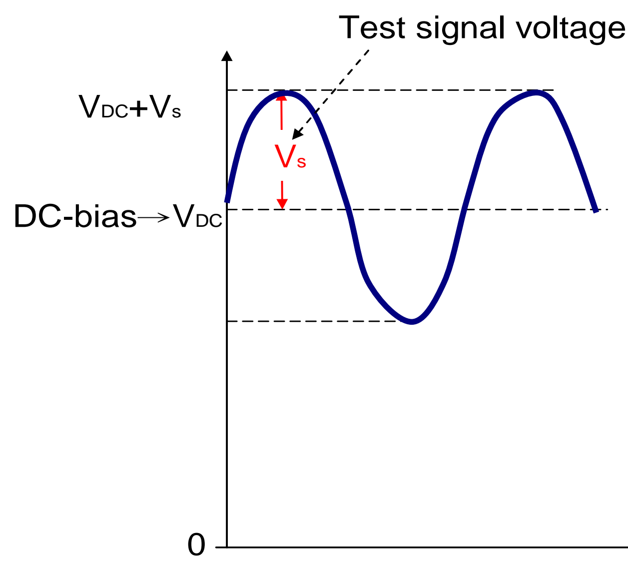

Figure 17 The input voltage signal in the capacitance-voltage measurement.

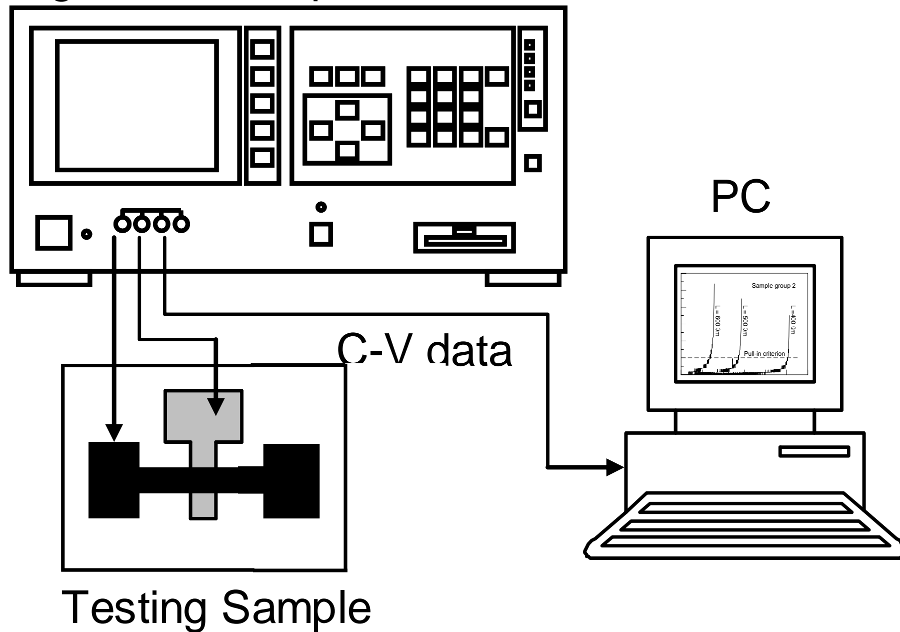

Figure 18 Schematic of the experiment setup for pull-in voltage detection.

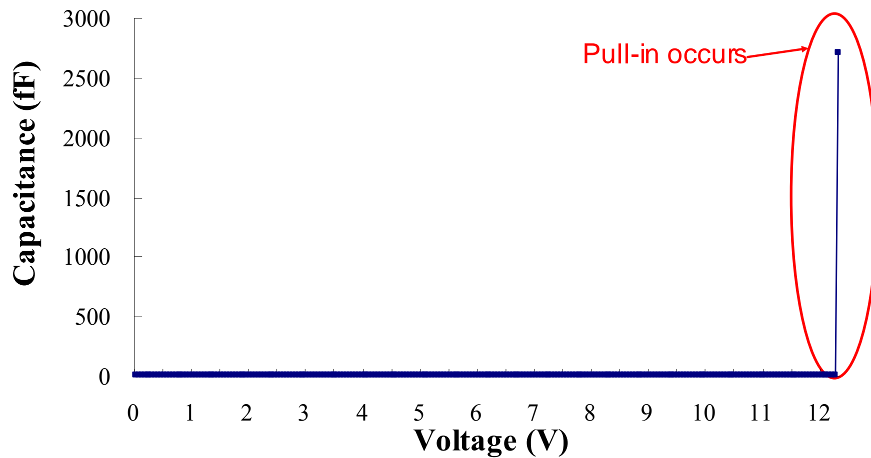

Figure 19 Typical sensitivities curves of the capacitances with respect to applied bias voltages of the test beam.

Table 5 Measurement conditions.

Function	Cp-D
Testing Signal Frequency	1 MHz
Testing Signal Level	0.025 V
Bias Voltage Range	0 – 40 V
Bias Voltage Step	0.05 V
Integration Time	Med

4.2.2 The Pull-in Voltage Results of Bridge-type Testkey

Table 6 lists the geometrical parameters of the bridge-type test beams which are fabricated by TSMC 0.18 μm 1P6M standard CMOS process. The test beams are with the same width, gap, and thickness but different length where the range is from 220μm to 300μm with 10μm period. Appendix A shows the measured capacitance-voltage curve results of each test beam with five times. One knows that pull-in occurs when capacitance is with sharp increase. According to Figure A-1 to Figure A-9 in Appendix A, it is obvious that the capacitance will raise up to tenfold even hundredfold value compared to the original capacitance when pull-in occurs. For example, Figure 20 shows the capacitances-voltage curve of the bridge-type testkey with L=230 μm. The capacitance before pull-in is about 19fF while about 1926fF when pull-in occurs which is hundredfold value compared to the original capacitance. Thus, one can obtain the pull-in voltage (V_{PI}) is 11.56V. Similarly, one can get the pull-in voltage of other test beams, the corresponding data is shown in Table 7 where $V_{PI\text{-}ave}$ is the average value of measured pull-in voltage for five times of each test beam, and ΔV_{PI} is the corresponding standard deviation. Figure 21 reveals the measured pull-in voltage results of each beam, the dark circle points point out the average pull-in voltage value, and the error bar indicate the standard deviation of each beam.

Table 6 Geometrical parameters of the bridge-type test beams.

Parameters	Values
Beam width b (μm)	5
Initial gap g (μm)	1.93
Beam thickness h (μm)	0.53
Beam length L (μm)	220-300

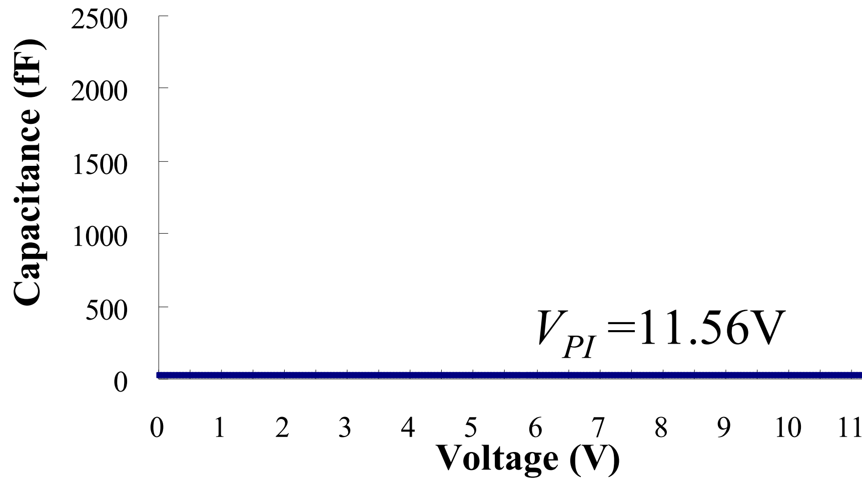

Figure 20 Capacitances-voltage curve of the bridge-type testkey with L=230 μm (V_{PI}=11.56V).

Table 7 The average and standard deviation of pull-in voltage value of each test beam.

Number	Width b (μm)	Length L (μm)	Vpull-in V_{PI}(V)	Average $V_{PI\text{-}ave}$ (V)	Standard Deviation $\triangle V_{PI}$
1	5	220	12.27,12.32,12.32,12.47,12.82	12.44	0.20
2	5	230	11.56,11.71,11.76,12.27,12.37	11.93	0.32
3	5	240	10.91,11.41,11.46,11.51,11.56	11.36	0.23
4	5	250	9.76,10.46,10.71,10.91,11.11	10.59	0.47
5	5	260	9.76,10.06,10.16,10.26,10.56	10.16	0.26
6	5	270	9.01, 9.11,9.52, 9.71, 9.96	9.46	0.36
7	5	280	8.81, 8.86,8.86 ,9.16, 9.51	9.04	0.27
8	5	290	8.06, 8.61, 8.86, 8.86,9.51	8.78	0.47
9	5	300	8.06 ,8.11, 8.31, 8.56,8.61	8.33	0.22

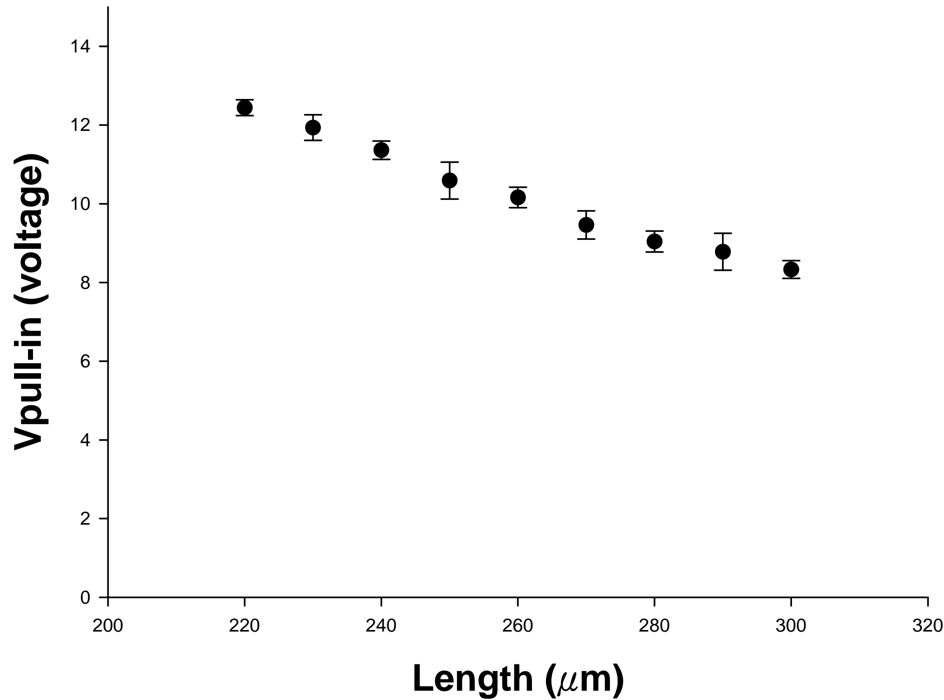

Figure 21 The average and standard deviation of pull-in voltage value of each test beam.

4.3 The Pre-deformation of Cantilever-type Testkey

Table 8 lists the geometrical parameters of the cantilever-type test beam which is fabricated by TSMC 0.18 μm 1P6M standard CMOS process. The cantilever-type test beam is made by metal 2. The author uses White Light Interfrometer (WLI) to determine the deformation curve of the cantilever-type testkey after post-process (Figure 22) and then fits the data by commercial software Matlab to obtain the shape function (Figure 23). Since one has known the shape function which is in quadratic parabolic form, and the maximum deflection (y_{max}) at the free end can be obtained. Table 9 lists the measured results of five different cantilever-type test beams with the same geometrical parameters.

Table 8   Geometrical parameters of the cantilever-type test beam.

Parameters	**Values**
Beam width b (μm)	5
Initial gap g (μm)	1.93
Beam thickness h (μm)	0.53
Beam length L (μm)	70

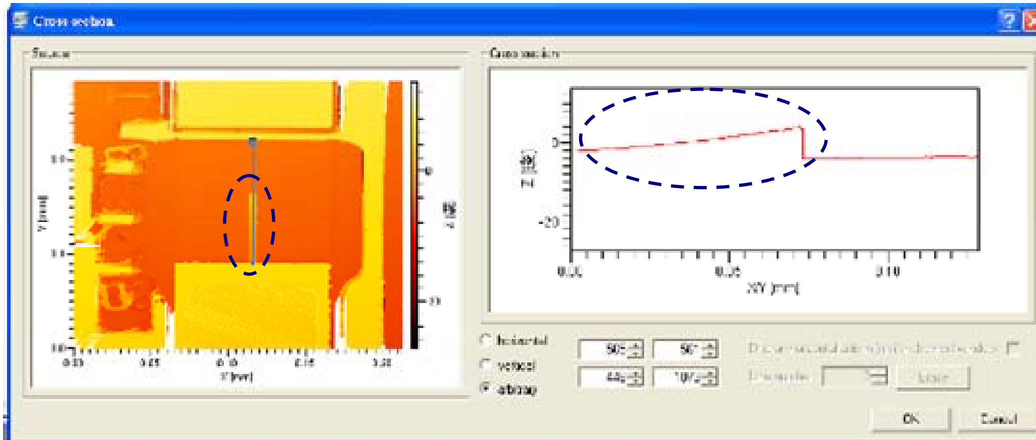

Figure 22   Deformation curve of the cantilever-type testkey detected by WLI.

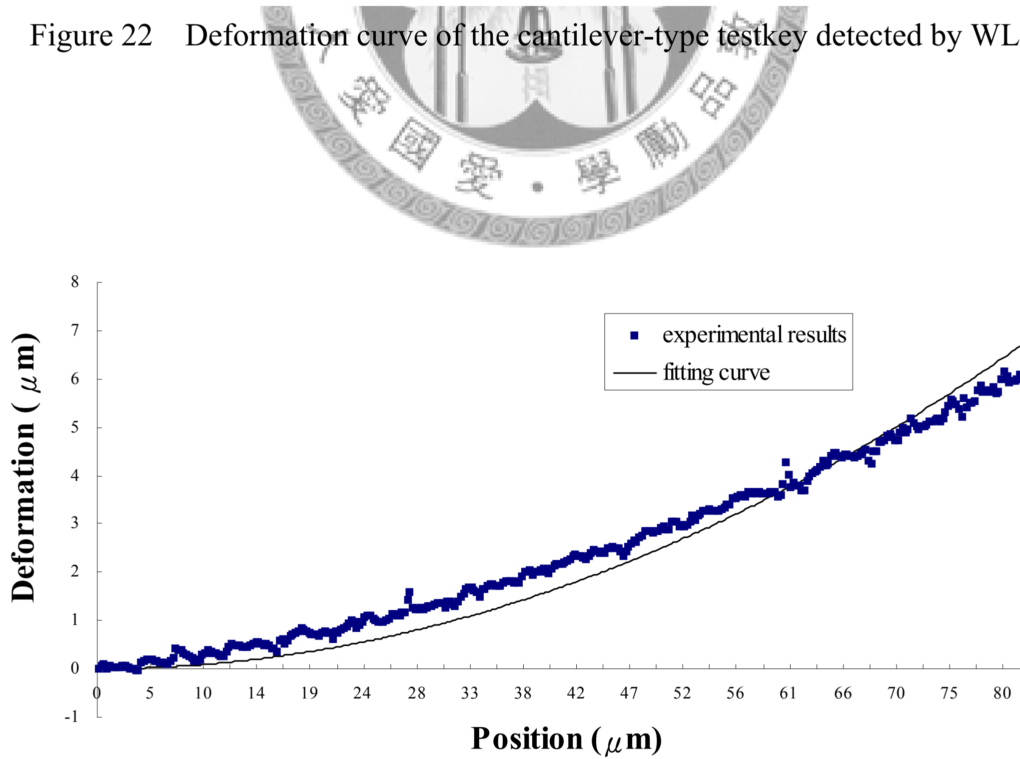

Figure 23   Shape function fitting by the commercial software Matlab.

Table 9 The measured results of cantilever-type test beams.

Width b (μm)	Length L (μm)	Shape Function	Location At Free End x_{max}(μm)	Maximum Deflection y_{max}(μm)
5	70	$y=0.00107x^2$	83.09	7.3877
5	70	$y= 0.001041x^2$	79.91	6.6478
5	70	$y= 0.001049x^2$	81.90	7.0371
5	70	$y= 0.0009811x^2$	81.10	6.4525
5	70	$y= 0.001017x^2$	81.02	6.6763

4.4 Extracting Mechanical Properties of Structural Material

The author selected two bridge-type beams at a time and substituted the experimental results (Table 7) into equation (28) to extract Young's modulus ($\tilde{E}$) and mean stress ($\tilde{\sigma}_0$). Figure 24 shows the extracted Young's modulus ($\tilde{E}$) and mean stress ($\tilde{\sigma}_0$) of the test beams. The extracted Young's modulus ($\tilde{E}$) can be obtained according to the upper triangular table in Figure 24, while mean stress ($\tilde{\sigma}_0$) is based on lower triangular table. For example, if one chooses two bridge-type beams which are with 220μm and 280μm, the extracted Young's modulus ($\tilde{E}$) and mean stress ($\tilde{\sigma}_0$) are 111.01 GPa and 3.6 MPa, respectively. It indicates that the extracted values with small standard deviation for large ΔL cases but with large standard deviation for small ΔL cases. Table 10 lists the extracted Young's modulus ($\tilde{E}$) and mean stress ($\tilde{\sigma}_0$) for two bridge-type beams with length difference (ΔL) equal to 50μm. Extracted Young's modulus ($\tilde{E}$) and mean stress ($\tilde{\sigma}_0$) are 132.01±13.48 GPa and 3.4±0.15 MPa respectively. According to the extracted Young's modulus value and substituted the

experimental results of maximum deflection at the free end in Table 9 into equation (23) to extract gradient stress ($\tilde{\sigma}_1$). Table 11 shows the extracted gradient stress ($\tilde{\sigma}_1$) of the test beams. The extracted gradient stress ($\tilde{\sigma}_1$) is 97.67±4.75 MPa.

△L (μ m)	10	20	30	40	50	60	70	80

E (GPa)

220	230	240	250	260	270	280	290	300	Length (μ m)
	-17.94	14	83.59	70.7	112.75	111.01	90.03	105.65	220
		50.3	50.94	108.6	157.04	147.87	120.85	133.52	230
			252.43	143.6	202.23	180.55	140.74	154.06	240
				20.95	172.29	219.68	103.75	126.68	250
					342.16	227.09	138.18	161.34	260
						98.49	18.1	86.72	270
							-71.39	79.84	280
								247.55	290
									300

Length (μ m)	220	230	240	250	260	270	280	290	300
220									
230	6.13								
240	5.51	4.91							
250	4.14	6.19	1.56						
260	4.39	3.86	3.36	5.09					
270	3.56	2.98	2.39	2.78	0.56				
280	3.6	3.15	2.75	4.12	2.19	3.75			
290	3.95	3.64	3.41	3.83	3.44	4.8	5.81		
300	3.7	3.41	3.19	3.48	3.11	3.9	3.97	2.2	

σ 0 (MPa)

Figure 24 The extracted Young's modulus and mean stress of the test beams.

Table 10 Extracted Young's modulus and mean stress of structural material fabricated by TSMC 0.18 μm 1P6M standard CMOS process.

Length difference (μm)	**Length** (μm)		**The extracted values by this work**	
ΔL	L_1	L_2	E (GPa)	σ_0 (MPa)
50	220	270	112.75	3.56
50	230	280	147.87	3.15
50	240	290	140.74	3.41
50	250	300	126.68	3.48
Average (X_{ave})			132.01	3.40
Standard Deviation (ΔX)			13.48	0.15
$\Delta X / X_{ave}$			10.21%	4.52%

Table 11 Extracted gradient stress of structural material fabricated by TSMC 0.18 μm 1P6M standard CMOS process.

Width b (μm)	**Length** L (μm)	**Maximum Deflection** y_{max}(μm)	**Gradient Stress** σ_1 (Mpa)
5	70	7.3877	105.49
5	70	6.6478	94.92
5	70	7.0371	100.48
5	70	6.4525	92.13
5	70	6.6763	95.33
Average (X_{ave})			97.67
Standard Deviation (ΔX)			4.75
$\Delta X / X_{ave}$			4.86%

The author has demonstrated our method to extract Young's modulus ($\tilde{E}$), mean stress ($\tilde{\sigma}_0$) and gradient stress ($\tilde{\sigma}_1$) of structural material fabricated by TSMC 0.18 μm 1P6M standard CMOS process. The overall deviation of the Young's modulus ($\tilde{E}$), mean stress ($\tilde{\sigma}_0$) and gradient stress ($\tilde{\sigma}_1$) of the demonstrated material are within 11% , 5%, and 4.86% respectively.

Chapter 5 Robustness Discussion

According to the results in chapter 4, it is obvious that measured pull-in voltage (V_{PI}) is with some deviation (ΔV_{PI}) and ΔL affects the extracted results, robustness discussion including sensitivity analysis for pull-in voltage measurement and dimension effects of testkey will be discussed in this chapter.

5.1 Sensitivity Analysis for Pull-in Voltage Measurement

This section presents how the variation in the pull-in voltage measurement of testkey can be attributed to different variations in the extracted structural material properties by using the algorithm in chapter 3. In other words, according to equation (28), the pull-in voltage variations ($V_{PI1} \pm \Delta V_{PI1}, V_{PI2} \pm \Delta V_{PI2}$) attributed to the variations in the extracted Young's modulus ($\tilde{E} \pm \Delta\tilde{E}$) and mean stress ($\tilde{\sigma}_0 \pm \Delta\tilde{\sigma}_0$) will be discussed in the functional form as equation (30) where V_{PI} is the average of the measured pull-in voltage results of each test beam with several times, ΔV_{PI} is the corresponding standard deviation, $\tilde{E}$ and $\tilde{\sigma}_0$ are the extracted Young's modulus and mean stress, $\Delta\tilde{E}$ and $\Delta\tilde{\sigma}_0$ are the corresponding variations, and the parameters *S* and *B* depend on the geometrical parameters of test beams in equation (31) and equation (34). There are four kinds of cases about the pull-in voltages (V_1 and V_2) of the two different bridge-type test beams:

(1) $V_1 = V_{PI1} + \Delta V_{PI1}, V_2 = V_{PI2} + \Delta V_{PI2}$,

(2) $V_1 = V_{PI1} - \Delta V_{PI1}, V_2 = V_{PI2} - \Delta V_{PI2}$,

(3) $V_1 = V_{PI1} - \Delta V_{PI1}, V_2 = V_{PI2} + \Delta V_{PI2}$,

(4) $V_1 = V_{PI1} + \Delta V_{PI1}, V_2 = V_{PI2} - \Delta V_{PI2}$.

Substituting the pull-in voltages of these four cases into equation (28), one can get the corresponding extracted material properties. In the following content, the variations about extracted values ($\Delta\tilde{E}_{(1)}$ to $\Delta\tilde{E}_{(4)}$ and $\Delta\tilde{\sigma}_{0(1)}$ to $\Delta\tilde{\sigma}_{0(4)}$) of these four cases will be derived.

$$\begin{Bmatrix} \tilde{\sigma}_0 \pm \Delta\tilde{\sigma}_0 \\ \tilde{E} \pm \Delta\tilde{E} \end{Bmatrix} = \begin{bmatrix} S_1 & B_1 \\ S_2 & B_2 \end{bmatrix}^{-1} \begin{Bmatrix} (V_{PI1} \pm \Delta V_{PI1})^2 \\ (V_{PI2} \pm \Delta V_{PI2})^2 \end{Bmatrix} \tag{30}$$

$$\begin{Bmatrix} \tilde{\sigma}_{0(1)} \\ \tilde{E}_{(1)} \end{Bmatrix} = \begin{bmatrix} S_1 & B_1 \\ S_2 & B_2 \end{bmatrix}^{-1} \begin{Bmatrix} (V_{PI1} + \Delta V_{PI1})^2 \\ (V_{PI2} + \Delta V_{PI2})^2 \end{Bmatrix} \tag{31}$$

$$\begin{Bmatrix} \tilde{\sigma}_{0(2)} \\ \tilde{E}_{(2)} \end{Bmatrix} = \begin{bmatrix} S_1 & B_1 \\ S_2 & B_2 \end{bmatrix}^{-1} \begin{Bmatrix} (V_{PI1} - \Delta V_{PI1})^2 \\ (V_{PI2} - \Delta V_{PI2})^2 \end{Bmatrix} \tag{32}$$

$$\begin{Bmatrix} \tilde{\sigma}_{0(3)} \\ \tilde{E}_{(3)} \end{Bmatrix} = \begin{bmatrix} S_1 & B_1 \\ S_2 & B_2 \end{bmatrix}^{-1} \begin{Bmatrix} (V_{PI1} - \Delta V_{PI1})^2 \\ (V_{PI2} + \Delta V_{PI2})^2 \end{Bmatrix} \tag{33}$$

$$\begin{Bmatrix} \tilde{\sigma}_{0(4)} \\ \tilde{E}_{(4)} \end{Bmatrix} = \begin{bmatrix} S_1 & B_1 \\ S_2 & B_2 \end{bmatrix}^{-1} \begin{Bmatrix} (V_{PI1} + \Delta V_{PI1})^2 \\ (V_{PI2} - \Delta V_{PI2})^2 \end{Bmatrix} \tag{34}$$

From equation (28), the extracted value of Young's modulus ($\tilde{E}$) and mean stress ($\tilde{\sigma}_0$) resulted from the average of the measured pull-in voltage results (V_{PI}) can be given as

$$\tilde{E} = \frac{S_2 V_{PI1}^2 - S_1 V_{PI2}^2}{S_2 B_1 - S_1 B_2}, \tag{35}$$

$$\tilde{\sigma}_0 = \frac{B_2 V_{PI1}^2 - B_1 V_{PI2}^2}{S_1 B_2 - S_2 B_1}. \tag{36}$$

Furthermore, equation (31) can be rearranged as

$$\tilde{E}_{(1)} = \frac{S_2(V_{PI1}+\Delta V_{PI1})^2 - S_1(V_{PI2}+\Delta V_{PI2})^2}{S_2B_1 - S_1B_2}, \tag{37}$$

$$\tilde{\sigma}_{0(1)} = \frac{B_2(V_{PI1}+\Delta V_{PI1})^2 - B_1(V_{PI2}+\Delta V_{PI2})^2}{S_1B_2 - S_2B_1}. \tag{38}$$

Subtracting equation (35) from equation (37), and one can get

$$\Delta\tilde{E}_{(1)} = \frac{S_2V_{PI1}^2[2(\frac{\Delta V_{PI1}}{V_{PI1}}) + (\frac{\Delta V_{PI1}}{V_{PI1}})^2] - S_1V_{PI2}^2[2(\frac{\Delta V_{PI2}}{V_{PI2}}) + (\frac{\Delta V_{PI2}}{V_{PI2}})^2]}{S_2B_1 - S_1B_2}. \tag{39}$$

Subtracting equation (36) from equation (38), and one can get

$$\Delta\tilde{\sigma}_{0(1)} = \frac{B_2V_{PI1}^2[2(\frac{\Delta V_{PI1}}{V_{PI1}}) + (\frac{\Delta V_{PI1}}{V_{PI1}})^2] - B_1V_{PI2}^2[2(\frac{\Delta V_{PI2}}{V_{PI2}}) + (\frac{\Delta V_{PI2}}{V_{PI2}})^2]}{S_1B_2 - S_2B_1}. \tag{40}$$

Since $\frac{\Delta V_{PI}}{V_{PI}}$ is smaller than 1, the author neglect the high order term $\left(\frac{\Delta V_{PI}}{V_{PI}}\right)^2$, and then obtain

$$\Delta\tilde{E}_{(1)} = \frac{S_2(2\Delta V_{PI1}V_{PI1}) - S_1(2\Delta V_{PI2}V_{PI2})}{S_2B_1 - S_1B_2}, \tag{41}$$

$$\Delta\tilde{\sigma}_{0(1)} = \frac{B_2(2\Delta V_{PI1}V_{PI1}) - B_1(2\Delta V_{PI2}V_{PI2})}{S_1B_2 - S_2B_1}. \tag{42}$$

Similarly,

$$\Delta\tilde{E}_{(2)} = \frac{-S_2(2\Delta V_{PI1}V_{PI1}) + S_1(2\Delta V_{PI2}V_{PI2})}{S_2B_1 - S_1B_2} = -\Delta\tilde{E}_{(1)}, \tag{43}$$

$$\Delta\tilde{\sigma}_{(2)} = \frac{-B_2(2\Delta V_{PI1}V_{PI1}) + B_1(2\Delta V_{PI2}V_{PI2})}{S_1B_2 - S_2B_1} = -\Delta\tilde{\sigma}_{(1)}, \tag{44}$$

$$\Delta\tilde{E}_{(3)} = \frac{-S_2(2\Delta V_{PI1}V_{PI1}) - S_1(2\Delta V_{PI2}V_{PI2})}{S_2B_1 - S_1B_2}, \tag{45}$$

$$\Delta\tilde{\sigma}_{(3)} = \frac{-B_2(2\Delta V_{PI1}V_{PI1}) - B_1(2\Delta V_{PI2}V_{PI2})}{S_1B_2 - S_2B_1}, \tag{46}$$

$$\Delta\tilde{E}_{(4)} = \frac{S_2(2\Delta V_{PI1}V_{PI1}) + S_1(2\Delta V_{PI2}V_{PI2})}{S_2B_1 - S_1B_2} = -\Delta\tilde{E}_{(3)}, \tag{47}$$

$$\Delta\tilde{\sigma}_{(4)} = \frac{B_2(2\Delta V_{PI1}V_{PI1}) + B_1(2\Delta V_{PI2}V_{PI2})}{S_1B_2 - S_2B_1} = -\Delta\tilde{\sigma}_{(3)}. \tag{48}$$

According to equations (41) to (48), it is obvious that

$$\left|\Delta\tilde{E}_{(4)}\right| = \left|\Delta\tilde{E}_{(3)}\right| > \left|\Delta\tilde{E}_{(1)}\right| = \left|\Delta\tilde{E}_{(2)}\right|, \tag{49}$$

$$\left|\Delta\tilde{\sigma}_{0(4)}\right| = \left|\Delta\tilde{\sigma}_{0(3)}\right| > \left|\Delta\tilde{\sigma}_{0(1)}\right| = \left|\Delta\tilde{\sigma}_{0(2)}\right|. \tag{50}$$

Therefore, the extracted values of Young's modulus $\tilde{E}$ and mean stress $\tilde{\sigma}_0$ with maximum variation $\Delta\tilde{E}$ and $\Delta\tilde{\sigma}_0$ are shown as

$$\Delta\tilde{E} = \frac{S_2(2\Delta V_{PI1}V_{PI1}) + S_1(2\Delta V_{PI2}V_{PI2})}{S_2 B_1 - S_1 B_2}, \tag{51}$$

$$\Delta\tilde{\sigma}_0 = \frac{B_2(2\Delta V_{PI1}V_{PI1}) + B_1(2\Delta V_{PI2}V_{PI2})}{S_1 B_2 - S_2 B_1}. \tag{52}$$

Substituting the measured value from Table 7 into equation (51) and equation (52), and the variations of the extracted Young's modulus ($\Delta\tilde{E}$) and mean stress ($\Delta\tilde{\sigma}_0$) can be obtained in Table 12. It indicates that the variation will decrease due to the increasing of corresponding denominator value of equation (51) when the difference of test beams ΔL increases. Since the difference of test beams ΔL is the important factor to affect the extracted variation, the dimension effects of testkeys will be discussed in the following section.

Table 12 The variations of the extracted Young's modulus and mean stress.

Length difference (μm)	**Length** (μm)		**Average** (V)		**Standard Deviation** (V)		**Variations of extracted values**		**Denominator of equation (51)**
ΔL	L_1	L_2	V_{PI1}	V_{PI2}	$\triangle V_{PI1}$	$\triangle V_{PI2}$	$\triangle E$ (GPa)	$\triangle\sigma_0$ (MPa)	$S_2 * B_1 - S_1 * B_2$
10	220	230	12.44	11.93	0.2	0.32	186.22	3.66	1.10E-15
30	220	250	12.44	10.59	0.2	0.47	107.60	2.12	2.46E-15
50	220	270	12.44	9.46	0.2	0.36	57.65	1.13	3.15E-15

5.2 Dimension Effects of Testkeys

According to the experimental results of published work [9] and the measured results shown in chapter 4 about the pull-in voltages of bridge-type test beams, this section reveals robustness discussion in dimension effects of testkeys. Table 2 lists the

geometrical parameters and Figures 25 and 26 show the measured pull-in voltages of the fixed-fixed beams which are made of mono-crystalline silicon in published work [9]. The author selected any two beams and substituted the measured data and beam dimensions into equation (28) to extract Young's modulus ($\tilde{E}$) and mean stress ($\tilde{\sigma}_0$), and the results shown in Figures 27 and 28. According to the extracted results shown Figures 24, 27, and 28, it indicates that the extracted values with small standard deviation for large ΔL cases but with large standard deviation for small ΔL cases in two kinds of common structural materials, such as the material made by the TSMC 0.18 μm standard CMOS process, and mono-crystalline silicon in (100) and (110) orientations. The author describes these extracted values in the tables with the corresponding ΔL. According to the results shown Figures 24, 27, and 28, the relative outcomes are list in Appendix B. According to the tables in Appendix B, one can know the relationship between the difference of test beams ΔL and the variation of the extracted values by this work shown in Figure 29. It indicates that the variation of $\Delta E/E$ and $\Delta\sigma_0/\sigma_0$ will reduce in 15% for ΔL is larger than 50μm, even in 2% for ΔL equal to 225μm in mono-crystalline silicon testing cases. These evidences show that the algorithm present in this work is robust in extracting mechanical properties at wafer-level testing. Furthermore, Table 13 shows the extracted results for material made by mono-crystalline silicon with ΔL is equal to 50 μm. For example, the extracted Young's modulus, and mean stress are 164.84 GPa, and 11.45 MPa for mono-crystalline silicon in (110) while the two test beams are with length 175μm and 225μm, respectively; the extracted Young's modulus, and mean stress are 164.03 GPa, and 10.01 MPa while the two test beams are with length 500μm and 550μm, respectively. Therefore, one can know that ΔL dominates the convergence of $\Delta E/E$ and $\Delta\sigma_0/\sigma_0$, not the pull-in voltage of the testkey. It means that there are no sharp

different extracted results when the bridge-type testkey is designed in with high pull-in voltage (division-1 in Figure 30) or low pull-in voltage (division-2 in Figure 30) in the same ΔL condition. Therefore, testkeys can be designed with low pull-in voltage characteristic to avoid the damage due to applying large driving bias to make pull-in occur.

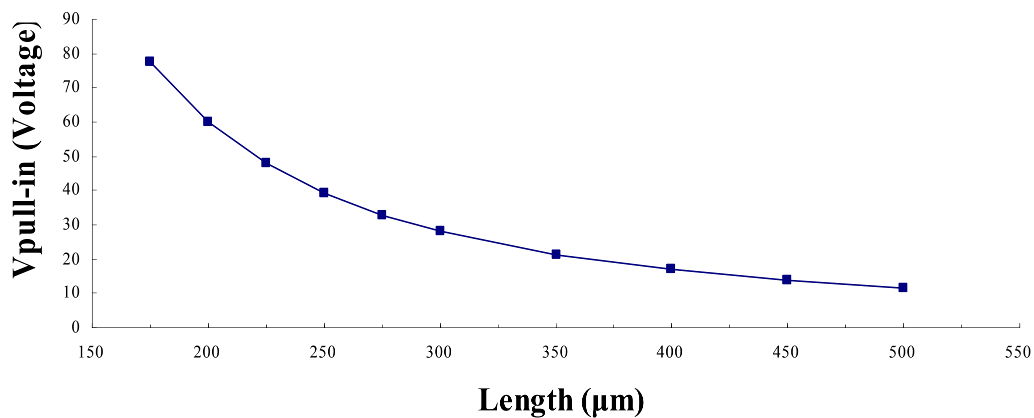

Figure 25 The measured the pull-in voltages of the fixed-fixed beams made of (100) mono-crystalline silicon in Osterberg's work [9].

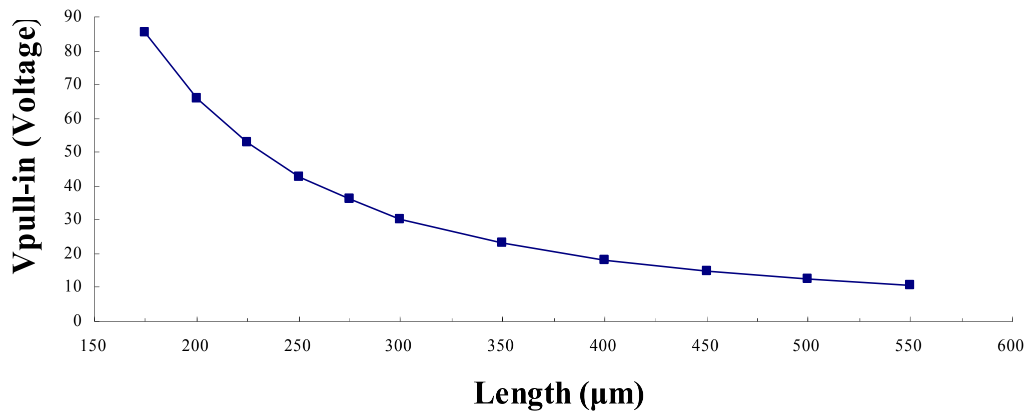

Figure 26 The measured the pull-in voltages of the fixed-fixed beams made of (100) mono-crystalline silicon in Osterberg's work [9].

△L (μm) 25 50 75 100 125 150 175 200 225 250 275 300 325

E (GPa)

Length (μm)	175	200	225	250	275	300	350	400	450	500
175		135.82	136.33	136.74	137.27	135.57	135.67	135.35	135.73	135.86
200			137.07	137.52	138.22	135.43	135.61	134.26	135.7	135.87
225				138.14	139.14	134.44	134.95	134.42	135.21	135.47
250					140.5	131.6	133.42	132.98	134.22	134.63
275						119.89	129.53	130	132.11	134.4
300							136.43	134.38	136.29	136.72
350								131.21	136.15	136.92
400									143.37	141.78
450										139.54
500										

σ0 (MPa)

Length (μm)	175	200	225	250	275	300	350	400	450	500
175										
200	9.52									
225	9.04	8.61								
250	8.65	8.28	7.99							
275	8.13	7.76	7.41	6.88						
300	9.76	9.81	10.13	11.05	14.87					
350	9.66	9.68	9.84	10.2	11.13	9.48				
400	9.97	10.67	10.14	10.41	10.95	10.15	10.73			
450	9.61	9.61	9.68	9.83	10.13	9.53	9.55	8.5		
500	9.49	9.49	9.53	9.63	9.66	9.39	9.36	8.79	9.06	

Figure 27 The extracted Young's modulus and mean stress of the test test beams made of (100) mono-crystalline silicon.

△L (μm) 25 50 75 100 125 150 175 200 225 250 275 300 325 350 375

E (GPa)

Length (μm)	175	200	225	250	275	300	350	400	450	500	550
175		169.28	164.84	167.3	166.2	167.98	167.05	167.07	166.88	166.66	166.6
200			158.35	165.62	165.35	167.25	166.04	166.16	165.96	165.71	165.66
225				175.77	168.88	172.66	169.52	169.2	168.66	168.16	167.99
250					159.56	170.27	166.53	166.67	166.24	165.78	165.68
275						184.35	170.36	169.5	168.48	167.65	167.4
300							160.32	163.05	163.05	162.29	162.81
350								167.24	165.54	164.37	164.32
400									163.05	161.92	162.42
450										160.34	161.91
500											164.03
550											

σ0 (MPa)

Length (μm)	175	200	225	250	275	300	350	400	450	500	550
175											
200	7.2										
225	11.45	15.21									
250	9.09	9.89	5.12								
275	10.15	10.48	9.11	12.73							
300	8.45	8.69	6.93	7.7	3.12						
350	9.33	9.57	8.74	9.46	8.54	10.94					
400	9.32	9.48	8.93	9.39	8.87	10.05	9.29				
450	9.5	9.63	9.24	9.59	9.27	10.05	9.69	10.05			
500	9.7	9.82	9.53	9.81	9.59	10.17	9.97	10.26	10.45		
550	9.76	9.86	9.63	9.85	9.69	10.13	9.99	10.17	10.22	10.01	

Figure 28 The extracted Young's modulus and mean stress of the test test beams made of (110) mono-crystalline silicon.

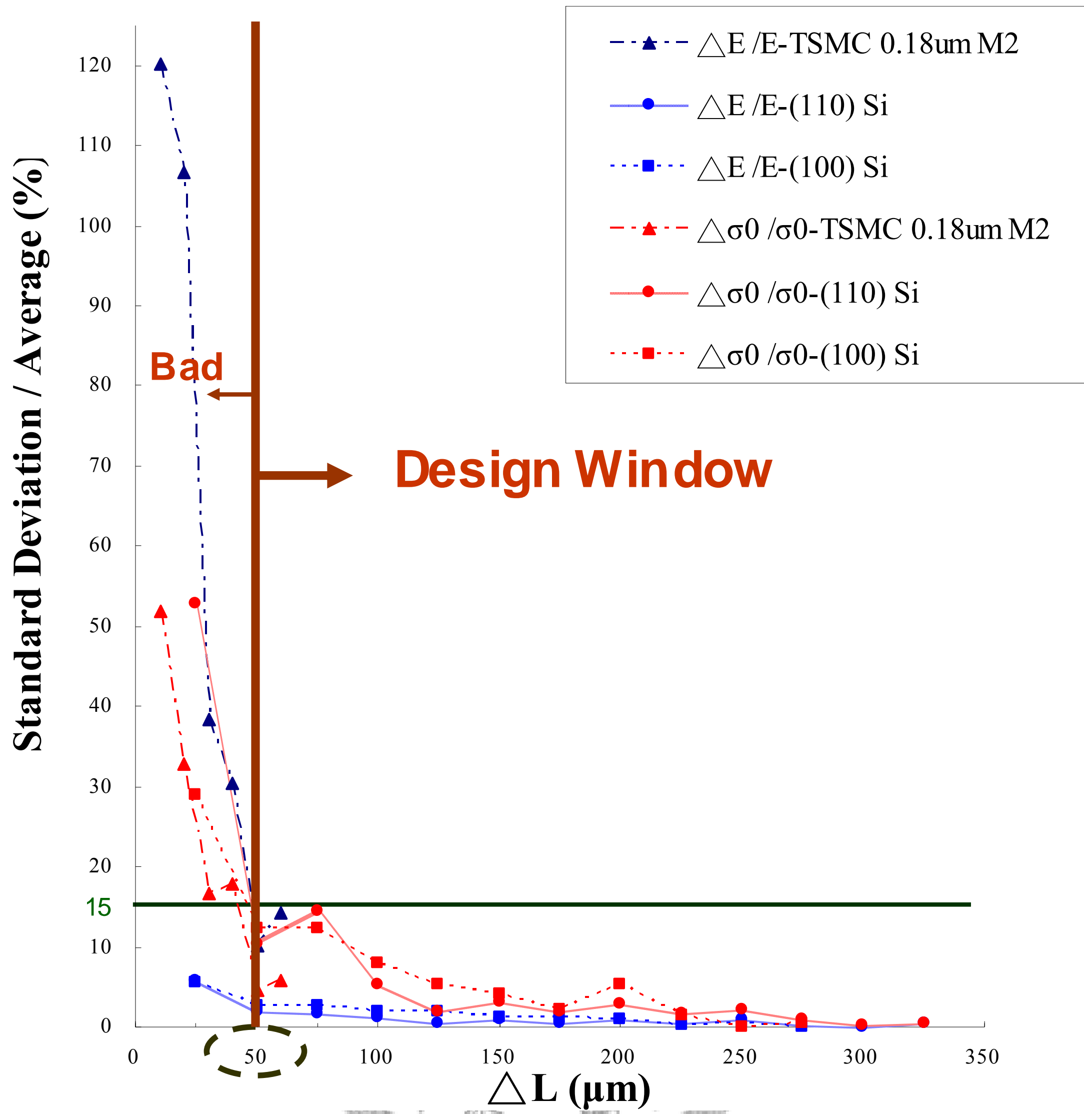

Figure 29 The variation of the extracted values by this work.

Table 13 The extracted results for material made by mono-crystalline silicon ($\triangle L$= 50 μm).

Crystal line plane of cross section	**Beam Length** (μm)		**The extracted values by this work**		**Average** (X_{ave})		**Standard Deviation** ($\triangle X$)		**Standard Deviation / Average** ($\triangle X/X_{ave}$)	
	L_1	L_2	E (GPa)	σ_0 (MPa)	E_{ave} (GPa)	$\sigma_{0\text{ave}}$ (MPa)	$\triangle E_{ave}$	$\triangle \sigma_{0\text{ave}}$	$\triangle E_{ave}/E_{ave}$	$\triangle \sigma_{0\text{ave}}/\sigma_{0\text{ave}}$
(100)	175	225	136.33	9.04	136.89	9.19	3.80	1.14	2.77%	12.42%
	200	250	137.52	8.28						
	225	275	139.14	7.41						
	250	300	131.6	11.05						
	300	350	136.43	9.48						
	350	400	131.21	10.73						
	400	450	143.37	8.5						
	450	500	139.54	9.06						
(110)	175	225	164.84	11.45	164.95	9.88	3.28	1.04	1.99%	10.49%
	200	250	165.62	9.89						
	225	275	168.88	9.11						
	250	300	170.27	7.7						
	300	350	160.32	10.94						
	350	400	167.24	9.29						
	400	450	163.05	10.05						
	450	500	160.34	10.45						
	500	550	164.03	10.01						

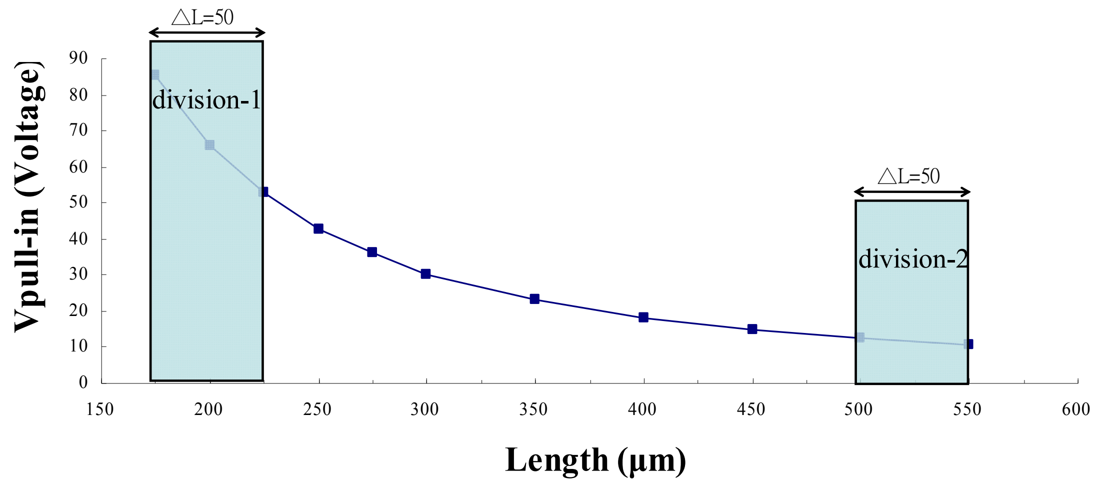

Figure 30 Testkeys design in the different divisions in the same △L condition.

Chapter 6 Conclusions

This dissertation presents a robust algorithm for extracting Young's modulus, mean stress, and gradient stress of structural materials of CMOS-MEMS devices. By detecting the pull-in voltages of two bridge-type test beams and the maximum deflection at the free end of the cantilever-type testkey, apply these characteristics to the equivalent electromechanical models, and one can know the mechanical properties of thin film. The contributions of this dissertation are described in detail as follows.

First, the author has demonstrated the present method with two common structural materials, such as the material made by the TSMC 0.18 μm standard CMOS process, and mono-crystalline silicon in (100) and (110) orientations. The extracted values by the present method are summarized in Table 14. The overall deviation of the extracted Young's modulus, mean stress, and gradient stress of the structural materials made by the TSMC 0.18 μm standard CMOS process are within 11% , 5%, and 4.86% respectively. Besides, the deviations of the extracted Young's modulus and mean stress are within 1 % and 2% which are almost tenth of the deviations of Osterberg's results [9] for mono-crystalline silicon in (100) and (110) orientations.

Table 14 The extracted results for common structural materials.

Common Structural Material	The extracted values by this work		
	E (GPa)	σ_0 (MPa)	σ_1 (MPa)
metal 2 made by the TSMC 0.18 μm standard CMOS process	132.01±13.48	3.4±0.15	97.67±4.75
mono-crystalline silicon in (100)	134.99±0.42	9.77±0.14	
mono-crystalline silicon in (110)	167.48±0.53	9.57±0.08	

Second, the study of robustness of present method including sensitivity analysis for pull-in voltage measurement and dimension effects of testkey is discussed in this dissertation. Moreover, this study also shows how the variation in the pull-in voltage measurement of testkey can be attributed to different variations in functional forms. For dimension effects of testkey, the variations of Young's modulus ($\Delta E/E$) and mean stress ($\Delta\sigma_0/\sigma_0$) are discussed, and the author inferences that the $\Delta E/E$ and $\Delta\sigma_0/\sigma_0$ will reduce within 15% for ΔL is larger than 50μm, even within 2% for ΔL larger than 225μm in mono-crystalline silicon testing cases according to the experimental results. Therefore, this study provides a recommended design window of testkey shown in Figure 29 for user.

Third, according to the results in this study, one can know that ΔL dominates the convergence of $\Delta E/E$ and $\Delta\sigma_0/\sigma_0$, not the pull-in voltage of the testkey. Therefore, testkeys can be designed with low pull-in voltage characteristic to avoid the damage

due to applying large driving bias to make pull-in occur.

Fourth, the testkeys can be set at the dicing path (Figure 31), and removed after testing. Therefore, it doesn't need the extra area to proceed structural material testing.

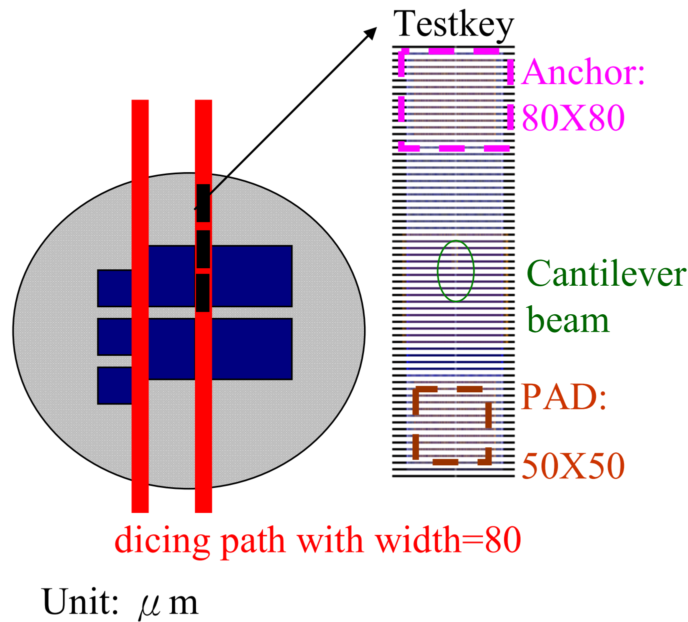

Figure 31 Testkeys set at the dicing path.

Fifth, the present method is very suitable for the implementation of the mechanical characterization of CMOS-MEMS devices on wafer level testing since the testing signals are non-destructive. Moreover, the present algorithm can easily be written as a programming code and accompanied by an LCR meter and WLI to realize the wafer-level testing for MEMS manufacture.

Chapter 7 Future Work

This dissertation has shown a method about CMOS-MEMS testkey for wafer-level mechanical properties extracting. However, this method has a constraint that the test material should be electric conduction, and it doesn't work for extracted the mechanical properties of dielectric material. One can use the present method and composite beam design shown by Dai's work [21] to obtain mechanical properties of the metal and dielectric layer. Second, the author apply LCR meter to get the information about capacitance versus applied voltage curve of the test beam and furthermore define the pull-in voltage. In the future, one can design a circuit with the testkey to detect the information of electric current versus applied voltage curve since the circuit will be short when pull-in occurs. Third, one can try to obtain the radius of curvature of cantilever-type testkey, and make this method to become a fully electric testing method. The present method just show a on-site wafer-level testing method, the author hope that through improving these disadvantages of present method, one can realize a method for real-time wafer-level testing.

Publication List of the Author

1. Y. C. Hu, P. Z. Chang, and **W. C. Chuang**, "An approximate analytical solution to the pull-in voltage of a micro bridge with an elastic boundary," *Journal of Micromechanics and Microengineering,* vol. 17, pp. 1870-1876, 2007.
2. Y.-C. Hu, J. H. Lin, K. Y. Huang, and **W. C. Chuang**, "An electrical testing method of the structural material of micro devices," *The Third Annual IEEE International Conference on Nano/Micro Engineered and Molecular Systems (IEEE NEMS 2008)*, Sanya-China, pp. 69-73, 2008.
3. **W. C. Chuang**, Y. C. Hu, C. Y. Lee, W. P. Shih, and P. Z. Chang, "Electromechanical behavior of the curled cantilever beam," *Journal of Micro-Nanolithography MEMS and MOEMS,* vol. 8, pp. 033020-033028, 2009.
4. **W. C. Chuang**, H. L. Lee, P. Z. Chang, and Y. C. Hu, "Review on the Modeling of Electrostatic MEMS," *Sensors,* vol. 10, pp. 6149-6171, 2010.
5. **W. C. Chuang**, H. L. Lee, T. W. Lin, Y. C. Hu, P. Z. Chang, and N. B. Quyen, "Optimal residual stress in CMOS fabrication," *The 34th National Conference on Theoretical and Applied Mechanics,* Yunlin-Taiwan, Nov. 19-20, 2010.
6. **W. C. Chuang**, C. W. Lin, Y. C. Hu, W. P. Shih, and P. Z. Chang, "An analytical model for optimizing LCD-cell design," *The 12th International Congress on Mesomechanics,* Taipei-Taiwan, June 21-25 ,2010.
7. **W. C. Chuang**, H. L. Lee, Y. C. Hu, W. P. Shih, and P. Z. Chang, "Electromechanical coupling of CMOS-MEMS testkey for extracting material properties," *The First IFToMM Asian Conference on Mechanism and Machine Science,* Taipei-Taiwan, October 21-25, 2010.
8. **W. C. Chuang**, Y. C. Hu, C. W. Wang, W. C. Chu ,and P. Z. Chang,"A Fringing Capacitance Model for Electrostatic Microstructure," *The 13th International Congress on Mesomechanics*, Vicenza-Italy, July 6-8, 2011.
9. W. C. Chu, **W. C. Chuang**, W. H. Tu, P. Z. Chang, and Y. C. Hu, "Etching holes effects for CMOS-MEMS capacitive structure," *International Conference on Adaptive Structures and Technologies*, Corfu –Greece, October 10-12 ,2011.

References

[1] H. K. Xie and G. K. Fedder, "Vertical comb-finger capacitive actuation and sensing for CMOS-MEMS," *Sensors and Actuators a-Physical,* vol. 95, pp. 212-221, 2002.

[2] Y. C. Cheng, C. L. Dai, C. Y. Lee, P. H. Chen, and P. Z. Chang, "A MEMS micromirror fabricated using CMOS post-process," *Sensors and Actuators A : Physical,* vol. 120, pp. 573-581, 2005.

[3] C. L. Dai, C. H. Kuo, and M. C. Chiang, "Microelectromechanical resonator manufactured using CMOS-MEMS technique," *Microelectronics Journal,* vol. 38, pp. 672-677, 2007.

[4] K. E. Petersen and C. R. Guarnieri, "Young's modulus measurements of thin films using micromechanics," *Journal of Applied Physics,* vol. 50, pp. 6761-6766, 1979.

[5] L. M. Zhang, D. Uttamchandani, and B. Culshaw, "Measurement of the mechanical properties of silicon microresonators," *Sensors and Actuators A: Physical,* vol. 29, pp. 79-84, 1991.

[6] L. Kiesewetter, J. M. Zhang, D. Houdeau, and A. Steckenborn, "Determination of Young's moduli of micromechanical thin films using the resonance method," *Sensors and Actuators A: Physical,* vol. 35, pp. 153-159, 1992.

[7] J. J. Vlassak and W. D. Nix, "New bulge test technique for the determination of Young's modulus and Poisson's ratio of thin films," *Journal of Materials Research,* vol. 7, pp. 3242-3249, 1992.

[8] Q. Zou, Z. Li, and L. Liu, "New methods for measuring mechanical properties of thin films in micromachining: beam pull-in voltage (V_{PI}) method and long beam deflection (LBD) method," *Sensors and Actuators A: Physical,* vol. 48, pp. 137-143, 1995.

[9] P. M. Osterberg and S. D. Senturia, "M-TEST: A test chip for MEMS material property measurement using electrostatically actuated test structures," *Journal of Microelectromechanical Systems,* vol. 6, pp. 107-118, 1997.

[10] W. N. Sharpe, Jr., B. Yuan, and R. L. Edwards, "New technique for measuring the mechanical properties of thin films," *Journal of Microelectromechanical Systems,* vol. 6, pp. 193-199, 1997.

[11] S. J. A. Johansson, L. Tenerz, and J. Tiren, "Fracture testing of silicon microelements in situ in a scanning electron microscope," *Journal of Applied Physics,* vol. 66, pp. 4799-4803, 1988.

[12] C. Serre, P. Gorostiza, A. Perez-Rodriguez, F. Sanz, and J. R. Morante, "Measurement of micromechanical properties of polysilicon microstructures

with an atomic force microscope," *Sensors and Actuators A: Physical,* vol. 67, pp. 215-219, 1998.

[13] C. Serre, A. Perez-Rodriguez, J. R. Morante, P. Gorostiza, and J. Esteve, "Determination of micromechanical properties of thin films by beam bending measurements with an atomic force microscope," *Sensors and Actuators A: Physical,* vol. 74, pp. 134-138, 1999.

[14] T. Chudoba, N. Schwarzer, F. Richter, and U. Beck, "Determination of mechanical film properties of a bilayer system due to elastic indentation measurements with a spherical indenter," *Thin Solid Films,* vol. 377-378, pp. 366-372, 2000.

[15] H. Guckel, D. Burns, C. Rutigliano, E. Lovell, and B. Choi, "Diagnostic microstructures for the measurement of intrinsic strain in thin films," *Journal of Micromechanics and Microengineering,* vol. 2, pp. 86-95, 1992.

[16] W. Fang and J. A. Wickert, "Comments on measuring thin-film stresses using bi-layer micromachined beams," *Journal of Micromechanics and Microengineering,* vol. 5, pp. 276-281, 1995.

[17] W. Fang and J. A. Wickert, "Determining mean and gradient residual stresses in thin films using micromachined cantilevers," *Journal of Micromechanics and Microengineering,* vol. 6, pp. 301-309, 1996.

[18] J.-A. Schweitz and F. Ericson, "Evaluation of mechanical materials properties by means of surface micromachined structures," *Sensors and Actuators A: Physical,* vol. 74, pp. 126-133, 1999.

[19] W. Fang and J. A. Wickert, "Post buckling of micromachined beams," *Journal of Micromechanics and Microengineering,* vol. 4, pp. 116-122, 1994.

[20] L. Riester, P. J. Blau, E. Lara-Curzio, and K. Breder, "Nanoindentation with a Knoop indenter," *Thin Solid Films,* vol. 377-378, pp. 635-639, 2000.

[21] C. L. Dai, "In situ electrostatic microactuators for measuring the Young's modulus of CMOS thin films," *Journal of Micromechanics and Microengineering,* vol. 13, pp. 563-567, 2003.

[22] J. C. Marshall, D. L. Herman, P. T. Vernier, D. L. DeVoe, and M. Gaitan, "Young's modulus measurements in standard IC CMOS processes using MEMS test structures," *IEEE Electron Device Letters,* vol. 28, pp. 960-963, 2007.

[23] X. Li, T. Ono, Y. Wang, and M. Esashi, "Ultrathin single-crystalline-silicon cantilever resonators: Fabrication technology and significant specimen size effect on Young's modulus," *Applied Physics Letters,* vol. 83, pp. 3081-3083, 2003.

[24] J. Yang, T. Ono, and M. Esashi, "Mechanical behavior of ultrathin

microcantilever," *Sensors and Actuators A: Physical,* vol. 82, pp. 102-107, 2000.

[25] S. A. Smee, M. Gaitan, D. B. Novotny, Y. Joshi, and D. L. Blackburn, "IC test structures for multilayer interconnect stress determination," *IEEE Electron Device Letters,* vol. 21, pp. 12-14, 2000.

[26] K. Najafi and K. Suzuki, "Novel technique and structure for the measurement of intrinsic stress and Young's modulus of thin films," *Micro Electro Mechanical Systems: An Investigation of Micro Structures, Sensors, Actuators, Machines and Robots*, Salt Lake City-USA, pp. 96-97, 1989.

[27] R. K. Gupta, P. M. Osterberg, and S. D. Senturia, "Material property measurements of micromechanical polysilicon beams," *Proceedings of SPIE - The International Society for Optical Engineering,* Austin-USA, pp. 39-45, 1996.

[28] W. C. Oliver and G. M. Pharr, "An improved technique for determining hardness and elastic modulus using load and displacement sensing indentation experiments," Journal of Materials Research, vol. 7, pp. 1564-1583, 1992.

[29] C. A. Klein, "How accurate are Stoney's equation and recent modifications," Journal of Applied Physics, vol. 88, pp. 5487-5489, 2000.

[30] P. Osterberg, H. Yie, X. Cai, J. White, and S. Senturia, "Self-consistent simulation and modeling of electrostatically deformed diaphragms," *Proceedings of the IEEE Micro Electro Mechanical Systems,* Oiso-Japen, pp. 28-32, 1994.

[31] E. S. Hung, Y.-J. Yang, and S. D. Senturia, "Low-order models for fast dynamical simulation of MEMS microstructures," *Proceedings of the 1997 International Conference on Solid-State Sensors and Actuators* , Chicago-USA, pp. 1101-1104, 1997.

[32] J. T. Stewart, "Finite element modeling of resonant microelectromechanical structures for sensing applications," *Proceedings of the 1994 IEEE Ultrasonics Symposium*, Cannes-France , pp. 643-646, 1994.

[33] N. R. Swart, S. F. Bart, M. H. Zaman, M. Mariappan, J. R. Gilbert, and D. Murphy, "AutoMM: Automatic generation of dynamic macromodels for MEMS devices," *Proceedings of the 1998 IEEE 11th Annual International Workshop on Micro Electro Mechanical Systems*, Heidelberg-Germany, pp. 178-183, 1998.

[34] T. Mukherjee, "Emerging simulation approaches for micromachined devices," *IEEE Transactions on Computer-Aided Design of Integrated Circuits and Systems,* vol. 19, p. 1572, 2000.

[35] R. M. Lin and W. J. Wang, "Structural dynamics of microsystems--current

state of research and future directions," *Mechanical Systems and Signal Processing,* vol. 20, pp. 1015-1043, 2006.

[36] C. W. Wang, "The interconnect fringing capacitance model and its applications to the study of pull-in Voltage of Micro Devices," Taipei, Taiwan: National Taiwan University-Master thesis, 2008.

[37] W. Soedel, *Vibrations of shells and plates*. New York: Marcel Dekker, 1993.

[38] M. R. Spiegel, *Mathematical Handbook of Formulas and Tables*. New York,USA: McGraw-Hill, 1987.

[39] F. P. Beer, E. R. Johnston, and J. T. DeWolf, *Mechanics of materials*. New York: McGraw-Hill, 1992.

Appendix A Capacitance-Voltage Measurement Results

Appendix A shows the measured capacitance-voltage curve results of each test beam with five times with the length equal from 220 μm to 290 μm. The test beams are fabricated by TSMC standard 1P6M process, and the geometrical parameters of bridge-type test beam are shown in table 6. The capacitance will raise up to tenfold even hundredfold value compared to the original capacitance when pull-in occurs. Thus, one can obtain the pull-in voltage (V_{PI}) for each test beam from the measured capacitance-voltage curve, and the results are summarized in table 7.

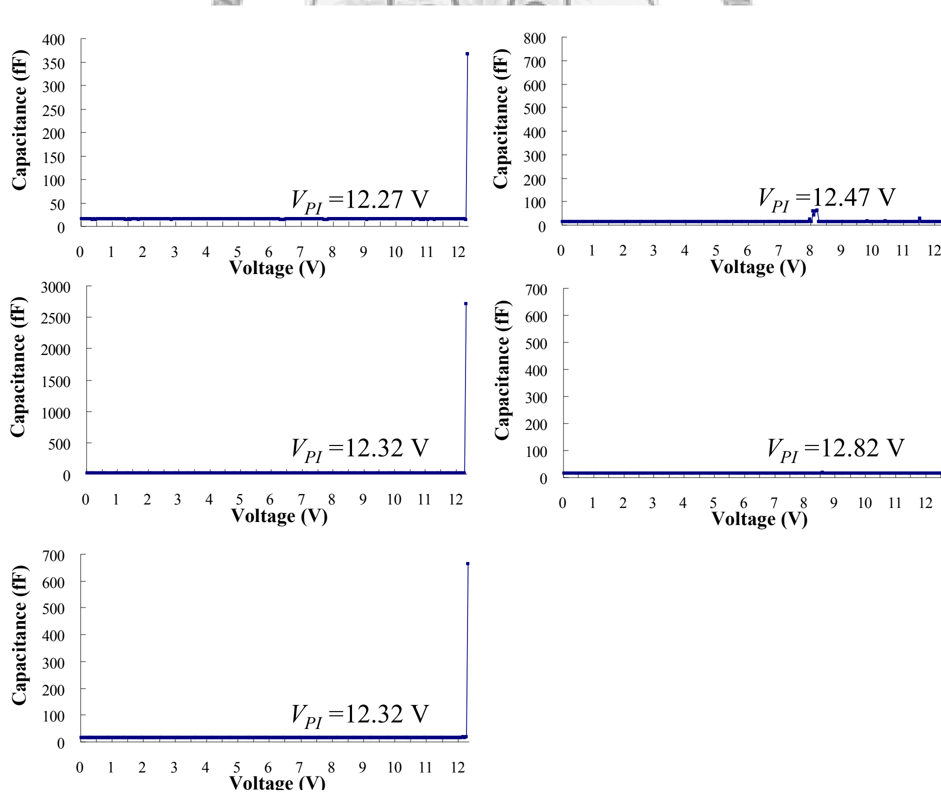

Figure A-1 Capacitances-voltage curve of the bridge-type testkey with L=220 μm.

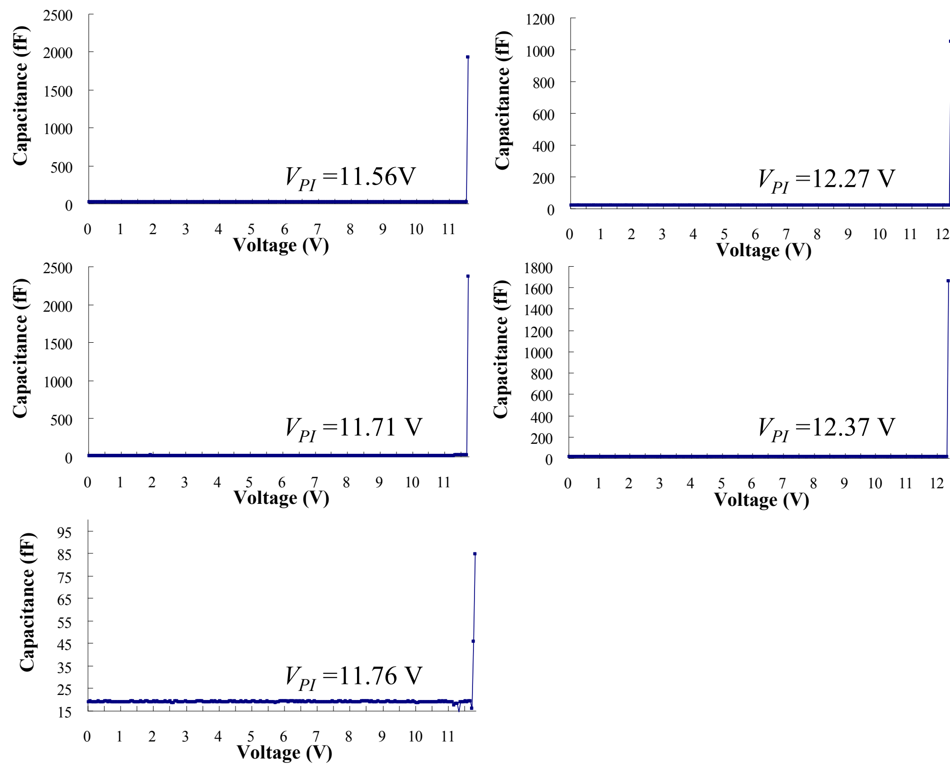

Figure A-2 Capacitances-voltage curve of the bridge-type testkey with L=230 μm.

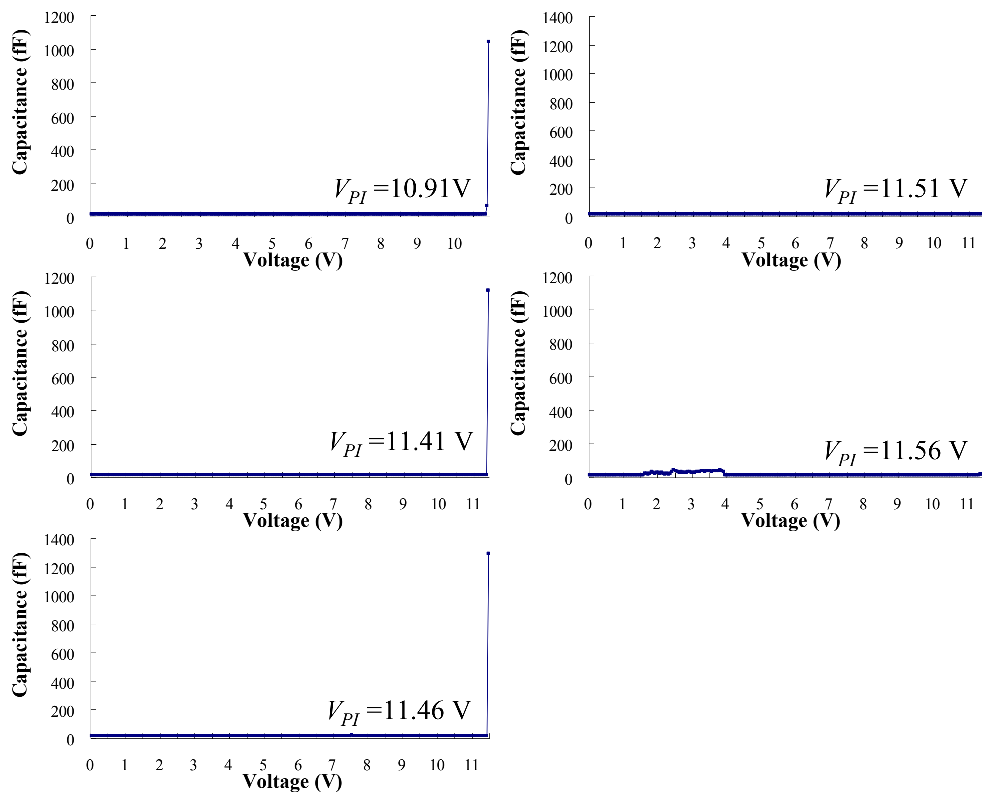

Figure A-3 Capacitances-voltage curve of the bridge-type testkey with L=240 μm.

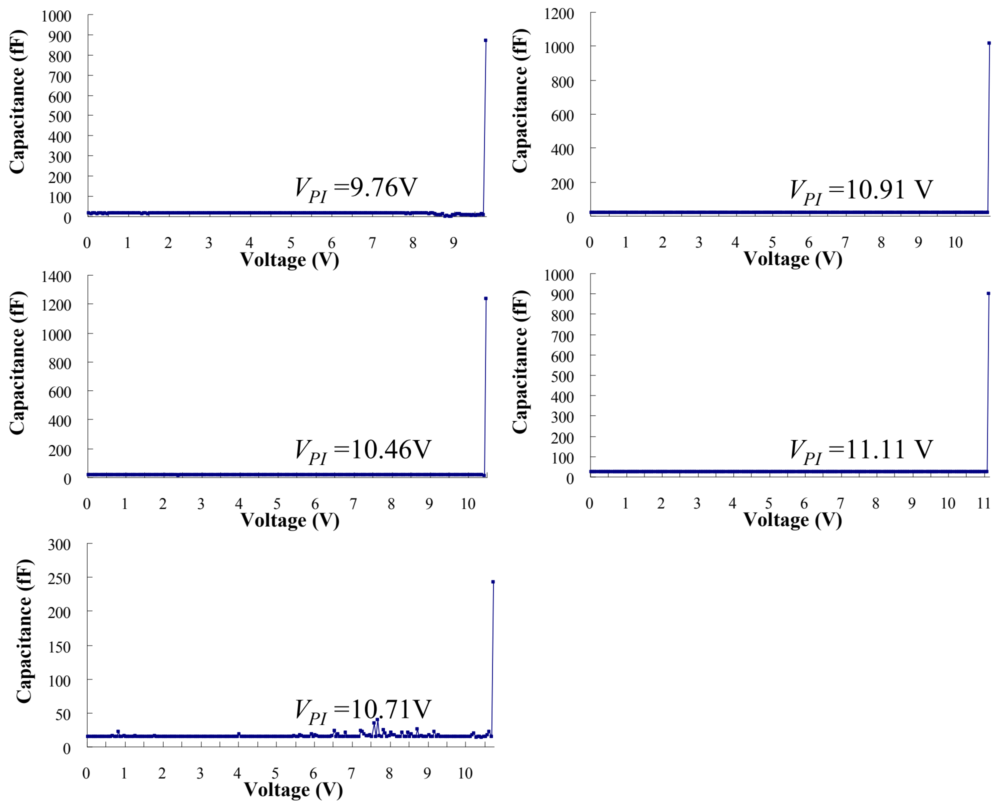

Figure A-4 Capacitances-voltage curve of the bridge-type testkey with L=250 μm.

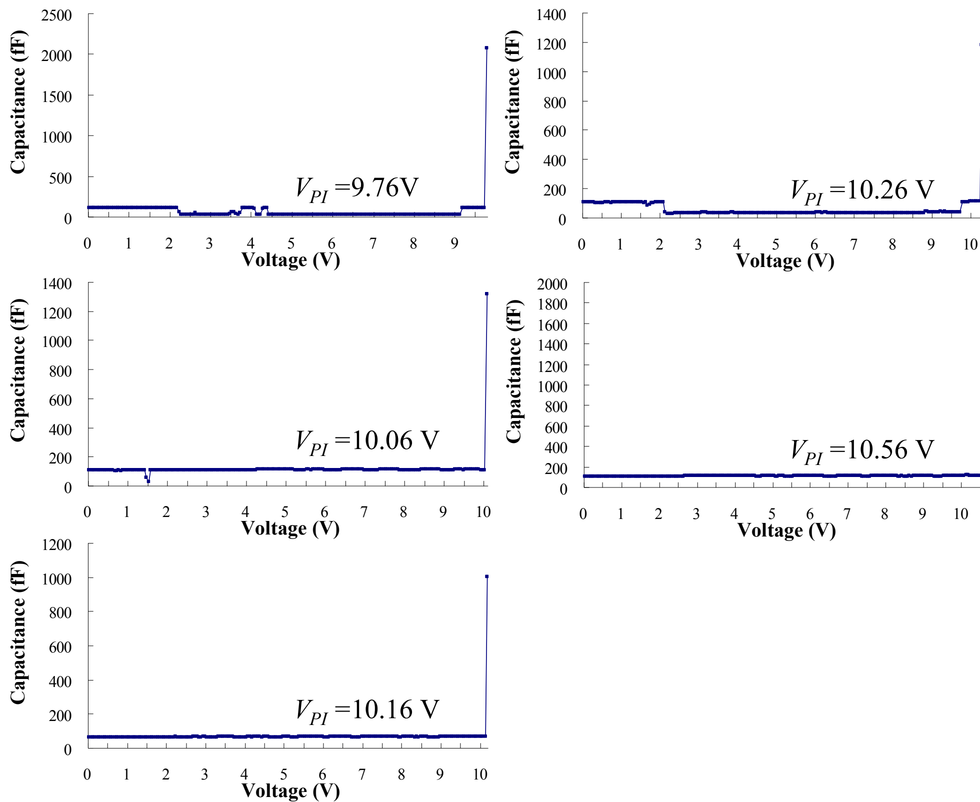

Figure A-5 Capacitances-voltage curve of the bridge-type testkey with L=260 μm.

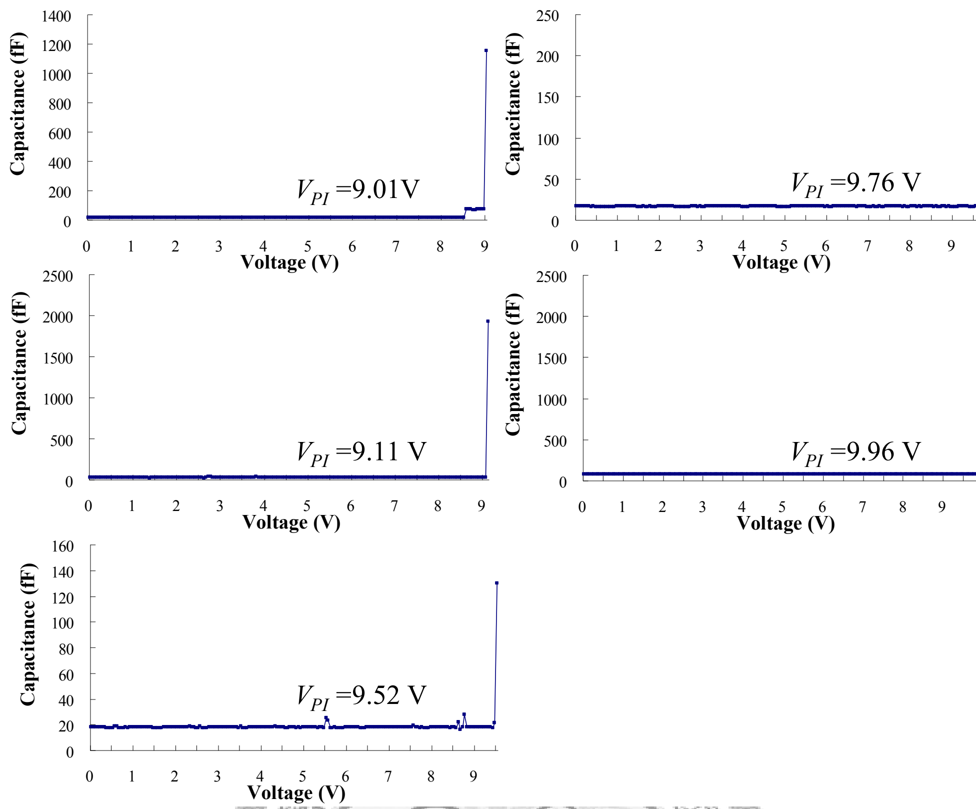

Figure A-6 Capacitances-voltage curve of the bridge-type testkey with L=270 μm.

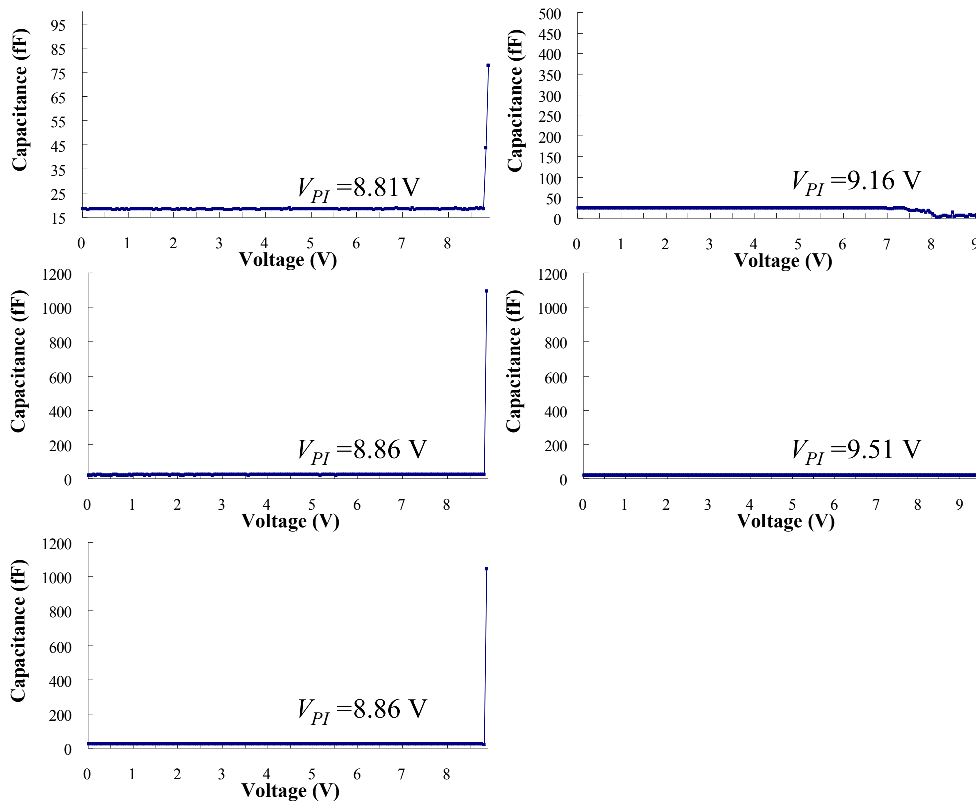

Figure A-7 Capacitances-voltage curve of the bridge-type testkey with L=280 μm.

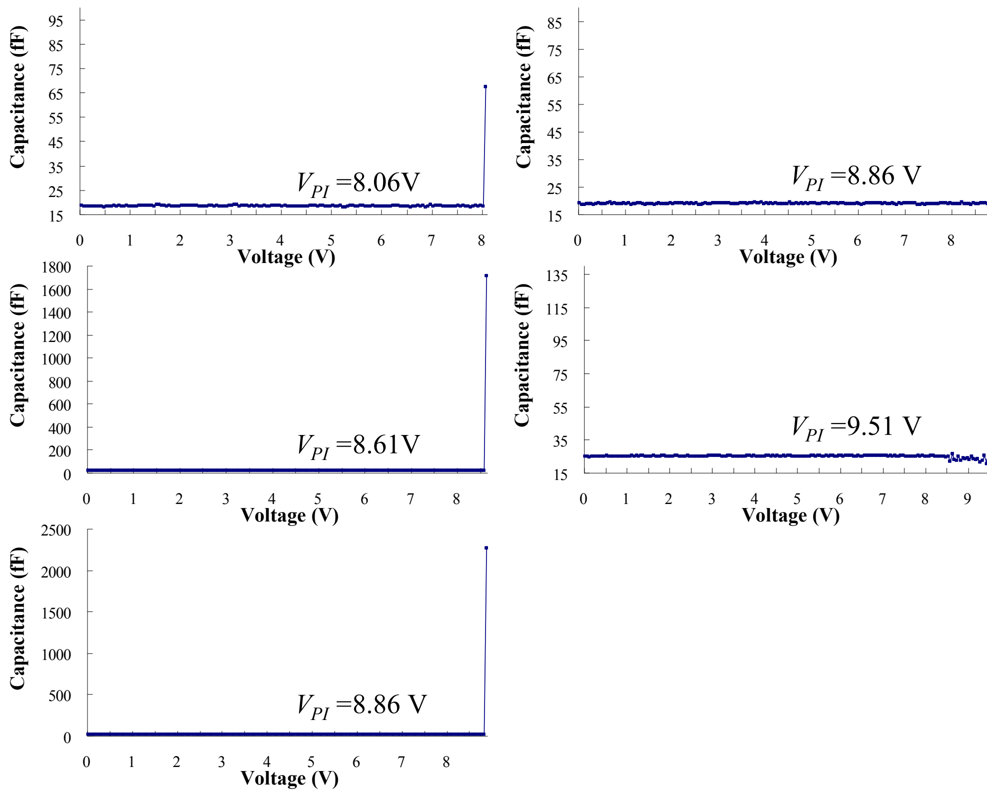

Figure A-8 Capacitances-voltage curve of the bridge-type testkey with L=290 μm.

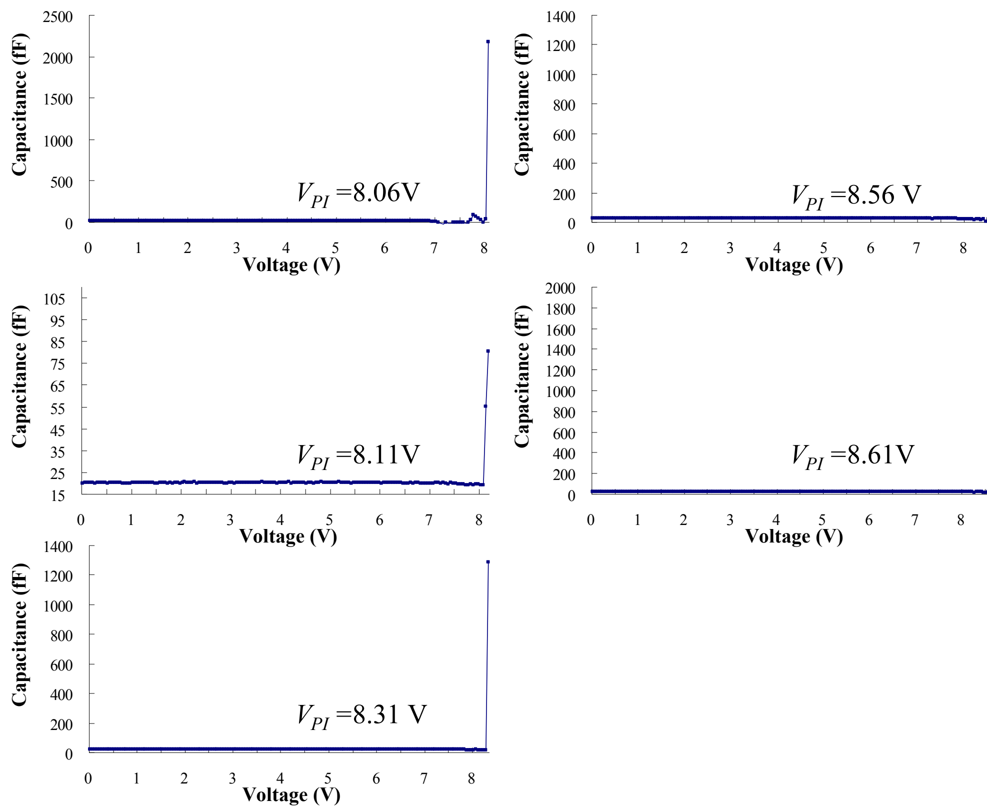

Figure A-9 Capacitances-voltage curve of the bridge-type testkey with L=300 μm.

Appendix B The Extracted Results for Common Materials

Table B-1 to table B-17 indicate that the extracted values with variations for different ΔL cases including the material made by the TSMC 0.18 μm standard CMOS process (table B-1 to table B-5), and mono-crystalline silicon in (100) and (110) orientations (table B-6 to table B-17). The results about the variation of extracted Young's modulus $\Delta E/E$ and mean stress $\Delta\sigma_0/\sigma_0$ are summarized in Figure 29.

Table B-1 The extracted results for material made by the TSMC 0.18 μm standard CMOS process ($\triangle L$= 10 μm).

Difference of test beams (μm)	**Beam Length** (μm)		**The extracted values by this work**	
$\triangle L$	L_1	L_2	E (GPa)	σ_0 (MPa)
10	220	230	-17.94	6.13
10	230	240	50.29	4.91
10	240	250	252.43	1.56
10	250	260	20.95	5.09
10	260	270	342.16	0.56
10	270	280	98.49	3.75
10	280	290	-71.39	5.81
10	290	300	247.55	2.20
Average (X_{ave})			115.32	3.75
Standard Deviation ($\triangle X$)			138.64	1.95
Standard Deviation / Average ($\triangle X/ X_{ave}$)			120.23%	51.99%

Table B-2 The extracted results for material made by the TSMC 0.18 μm standard CMOS process (△L= 20 μm).

Difference of test beams (μm)	**Beam Length** (μm)		**The extracted values by this work**	
△L	L_1	L_2	E (GPa)	σ_0 (MPa)
20	220	240	13.95	5.51
20	230	250	-50.94	6.19
20	240	260	143.63	3.36
20	250	270	172.29	2.78
20	260	280	227.09	2.19
20	270	290	18.10	4.80
20	280	300	79.84	3.97
Average (X_{ave})			86.28	4.11
Standard Deviation (△X)			92.01	1.35
Standard Deviation / Average (△X/ X_{ave})			106.65%	32.87%

Table B-3 The extracted results for material made by the TSMC 0.18 μm standard CMOS process (△L= 30 μm).

Difference of test beams (μm)	**Beam Length** (μm)		**The extracted values by this work**	
△L	L_1	L_2	E (GPa)	σ_0 (MPa)
30	220	250	83.59	4.14
30	230	260	108.61	3.86
30	240	270	202.23	2.39
30	250	280	219.68	4.12
30	260	290	138.18	3.44
30	270	300	86.72	3.90
Average (X_{ave})			139.84	3.64
Standard Deviation (△X)			53.59	0.61
Standard Deviation / Average (△X/ X_{ave})			38.32%	16.62%

Table B-4 The extracted results for material made by the TSMC 0.18 μm standard CMOS process (△L= 40 μm).

Difference of test beams (μm)	Beam Length (μm)		The extracted values by this work	
△L	L_1	L_2	E (GPa)	σ_0 (MPa)
40	220	260	70.70	4.39
40	230	270	157.04	2.98
40	240	280	180.55	2.75
40	250	290	103.75	3.83
40	260	300	161.34	3.11
Average (X_{ave})			134.68	3.41
Standard Deviation (△X)			40.90	0.61
Standard Deviation / Average (△X/ X_{ave})			30.37%	17.81%

Table B-5 The extracted results for material made by the TSMC 0.18 μm standard CMOS process (△L= 50 μm).

Difference of test beams (μm)	Beam Length (μm)		The extracted values by this work	
△L	L_1	L_2	E (GPa)	σ_0 (MPa)
50	220	270	112.75	3.56
50	230	280	147.87	3.15
50	240	290	140.74	3.41
50	250	300	126.68	3.48
Average (X_{ave})			132.01	3.40
Standard Deviation (△X)			13.48	0.15
Standard Deviation / Average (△X/ X_{ave})			10.21%	4.52%

Table B-6 The extracted results for material made by the TSMC 0.18 μm standard CMOS process (△L= 60 μm).

Difference of test beams (μm)	**Beam Length** (μm)		**The extracted values by this work**	
△L	L_1	L_2	E (GPa)	σ_0 (MPa)
60	220	280	111.01	3.60
60	230	290	120.85	3.64
60	240	300	154.06	3.19
Average (X_{ave})			128.64	3.48
Standard Deviation (△X)			18.42	0.20
Standard Deviation / Average (△X/ X_{ave})			14.32%	5.85%

Table B-7 The extracted results for material made by mono-crystalline silicon (△L= 25 μm).

Crystal line plane of cross section	**Beam Length** (μm)		**The extracted values by this work**		**Average** (X_{ave})		**Standard Deviation** (△X)		**Standard Deviation / Average** (△X/X_{ave})	
	L_1	L_2	E (GPa)	σ_0 (MPa)	E_{ave} (GPa)	$\sigma_{0\text{ave}}$ (MPa)	△E_{ave}	△$\sigma_{0\text{ave}}$	△E_{ave}/ E_{ave}	△$\sigma_{0\text{ave}}$ /$\sigma_{0\text{ave}}$
(100)	175	200	135.82	9.52	134.28	9.57	7.36	2.78	5.48%	29.08%
	200	225	137.07	8.61						
	225	250	138.14	7.99						
	250	275	140.5	6.88						
	275	300	119.89	14.87						
(110)	175	200	169.28	7.2	169.46	8.68	9.83	4.58	5.80%	52.77%
	200	225	158.35	15.21						
	225	250	175.77	5.12						
	250	275	159.56	12.73						
	275	300	184.35	3.12						

Table B-8 The extracted results for material made by mono-crystalline silicon ($\triangle L$= 50 μm).

Crystal line plane of cross section	**Beam Length** (μm)		**The extracted values by this work**		**Average** (X_{ave})		**Standard Deviation** ($\triangle X$)		**Standard Deviation / Average** ($\triangle X/X_{ave}$)	
	L_1	L_2	E (GPa)	σ_0 (MPa)	E_{ave} (GPa)	σ_{0ave} (MPa)	$\triangle E_{ave}$	$\triangle \sigma_{0ave}$	$\triangle E_{ave}/E_{ave}$	$\triangle \sigma_{0ave}/\sigma_{0ave}$
(100)	175	225	136.33	9.04	136.89	9.19	3.80	1.14	2.77%	12.42%
	200	250	137.52	8.28						
	225	275	139.14	7.41						
	250	300	131.6	11.05						
	300	350	136.43	9.48						
	350	400	131.21	10.73						
	400	450	143.37	8.5						
	450	500	139.54	9.06						
(110)	175	225	164.84	11.45	164.95	9.88	3.28	1.04	1.99%	10.49%
	200	250	165.62	9.89						
	225	275	168.88	9.11						
	250	300	170.27	7.7						
	300	350	160.32	10.94						
	350	400	167.24	9.29						
	400	450	163.05	10.05						
	450	500	160.34	10.45						
	500	550	164.03	10.01						

Table B-9 The extracted results for material made by mono-crystalline silicon ($\triangle L$= 75 μm).

Crystal line plane of cross section	**Beam Length** (μm)		**The extracted values by this work**		**Average** (X_{ave})		**Standard Deviation** ($\triangle X$)		**Standard Deviation / Average** ($\triangle X/X_{ave}$)	
	L_1	L_2	E (GPa)	σ_0 (MPa)	E_{ave} (GPa)	σ_{0ave} (MPa)	$\triangle E_{ave}$	$\triangle \sigma_{0ave}$	$\triangle E_{ave}/E_{ave}$	$\triangle \sigma_{0ave}/\sigma_{0ave}$
(100)	175	250	136.74	8.65	136.47	8.85	1.56	0.98	1.14%	11.05%
	200	275	138.22	7.76						
	225	300	134.44	10.13						
(110)	175	250	167.3	9.09	168.44	8.83	3.09	1.46	1.83%	16.54%
	200	275	165.35	10.48						
	225	300	172.66	6.93						

Table B-10 The extracted results for material made by mono-crystalline silicon ($\triangle L$= 100 μm).

Crystal line plane of cross section	**Beam Length** (μm)		**The extracted values by this work**		**Average** (X_{ave})		**Standard Deviation** ($\triangle X$)		**Standard Deviation / Average** ($\triangle X/X_{ave}$)	
	L_1	L_2	E (GPa)	σ_0 (MPa)	E_{ave} (GPa)	$\sigma_{0\text{ave}}$ (MPa)	$\triangle E_{ave}$	$\triangle\sigma_{0\text{ave}}$	$\triangle E_{ave}/E_{ave}$	$\triangle\sigma_{0\text{ave}}/\sigma_{0\text{ave}}$
(100)	175	275	137.27	8.13	136.41	9.44	2.70	0.75	1.98%	7.94%
	200	300	135.43	9.81						
	250	350	133.42	10.2						
	300	400	134.38	10.15						
	350	450	136.15	9.55						
	400	500	141.78	8.79						
(110)	175	275	166.2	10.15	164.63	9.79	2.10	0.53	1.28%	5.37%
	200	300	167.25	8.69						
	250	350	166.53	9.46						
	300	400	163.05	10.05						
	350	450	165.54	9.69						
	400	500	161.92	10.26						
	450	550	161.91	10.22						

Table B-11 The extracted results for material made by mono-crystalline silicon ($\triangle L$= 125 μm).

Crystal line plane of cross section	**Beam Length** (μm)		**The extracted values by this work**		**Average** (X_{ave})		**Standard Deviation** ($\triangle X$)		**Standard Deviation / Average** ($\triangle X/X_{ave}$)	
	L_1	L_2	E (GPa)	σ_0 (MPa)	E_{ave} (GPa)	σ_{0ave} (MPa)	$\triangle E_{ave}$	$\triangle \sigma_{0ave}$	$\triangle E_{ave}/E_{ave}$	$\triangle \sigma_{0ave}/\sigma_{0ave}$
(100)	175	300	135.57	9.76	133.51	10.18	2.49	0.54	1.87%	5.33%
	225	350	134.95	9.84						
	275	400	130	10.95						
(110)	175	300	167.98	8.45	169.00	8.69	0.72	0.18	0.43%	2.02%
	225	350	169.52	8.74						
	275	400	169.5	8.87						

Table B-12 The extracted results for material made by mono-crystalline silicon ($\triangle L$= 150 μm).

Crystal line plane of cross section	**Beam Length** (μm)		**The extracted values by this work**		**Average** (X_{ave})		**Standard Deviation** ($\triangle X$)		**Standard Deviation / Average** ($\triangle X/X_{ave}$)	
	L_1	L_2	E (GPa)	σ_0 (MPa)	E_{ave} (GPa)	σ_{0ave} (MPa)	$\triangle E_{ave}$	$\triangle \sigma_{0ave}$	$\triangle E_{ave}/E_{ave}$	$\triangle \sigma_{0ave}/\sigma_{0ave}$
(100)	200	350	135.61	9.68	135.45	9.75	1.50	0.40	1.11%	4.11%
	250	400	132.98	10.41						
	300	450	136.29	9.53						
	350	500	136.92	9.36						
(110)	200	350	166.04	9.57	164.51	9.83	1.64	0.30	1.00%	3.03%
	250	400	166.67	9.39						
	300	450	163.05	10.05						
	350	500	164.37	9.97						
	400	550	162.42	10.17						

Table B-13 The extracted results for material made by mono-crystalline silicon (△L= 175 μm).

Crystal line plane of cross section	Beam Length (μm)		The extracted values by this work		Average (X_{ave})		Standard Deviation (△X)		Standard Deviation / Average (△X/X_{ave})	
	L_1	L_2	E (GPa)	σ_0 (MPa)	E_{ave} (GPa)	σ_{0ave} (MPa)	△E_{ave}	△σ_{0ave}	△E_{ave}/E_{ave}	△$\sigma_{0ave}/\sigma_{0ave}$
(100)	175	350	135.67	9.66	135.67	9.66	1.47	0.22	1.10%	2.24%
	225	400	134.42	10.14						
	275	450	132.11	10.13						
	175	350	134.07	9.98						
(110)	175	350	167.05	9.33	168.24	9.18	0.89	0.18	0.53%	1.92%
	225	400	169.2	8.93						
	275	450	168.48	9.27						

Table B-14 The extracted results for material made by mono-crystalline silicon (△L= 200 μm).

Crystal line plane of cross section	Beam Length (μm)		The extracted values by this work		Average (X_{ave})		Standard Deviation (△X)		Standard Deviation / Average (△X/X_{ave})	
	L_1	L_2	E (GPa)	σ_0 (MPa)	E_{ave} (GPa)	σ_{0ave} (MPa)	△E_{ave}	△σ_{0ave}	△E_{ave}/E_{ave}	△$\sigma_{0ave}/\sigma_{0ave}$
(100)	200	400	134.26	10.67	135.07	9.96	1.17	0.53	0.87%	5.33%
	250	450	134.22	9.83						
	300	500	136.72	9.39						
(110)	200	400	166.16	9.48	166.16	9.48	1.62	0.28	0.98%	2.88%
	250	450	166.24	9.59						
	300	500	162.29	10.17						
	350	550	164.32	9.99						
	200	400	164.75	9.81						

Table B-15 The extracted results for material made by mono-crystalline silicon ($\triangle L$= 225 μm).

Crystal line plane of cross section	**Beam Length** (μm)		**The extracted values by this work**		**Average** (X_{ave})		**Standard Deviation** ($\triangle X$)		**Standard Deviation / Average** ($\triangle X/X_{ave}$)	
	L_1	L_2	E (GPa)	σ_0 (MPa)	E_{ave} (GPa)	σ_{0ave} (MPa)	$\triangle E_{ave}$	$\triangle \sigma_{0ave}$	$\triangle E_{ave}/E_{ave}$	$\triangle \sigma_{0ave}/\sigma_{0ave}$
(100)	175	400	135.35	9.97	134.99	9.77	0.42	0.14	0.31%	1.45%
	225	450	135.21	9.68						
	275	500	134.4	9.66						
(110)	175	400	167.07	9.32	167.79	9.38	0.66	0.15	0.39%	1.60%
	225	450	168.66	9.24						
	275	500	167.65	9.59						

Table B-16 The extracted results for material made by mono-crystalline silicon in (110) ($\triangle L$= 250 μm).

Difference of test beams (μm)	**Beam Length** (μm)		**The extracted values by this work**	
$\triangle L$	L_1	L_2	E (GPa)	σ_0 (MPa)
250	200	450	165.96	9.63
250	250	500	165.78	9.81
250	300	550	162.81	10.13
Average (X_{ave})			164.85	9.86
Standard Deviation ($\triangle X$)			1.44	0.21
Standard Deviation / Average ($\triangle X/ X_{ave}$)			0.88%	2.10%

Table B-17 The extracted results for material made by mono-crystalline silicon in (110) (△L= 275 μm).

Difference of test beams (μm)	Beam Length (μm)		The extracted values by this work	
△L	L_1	L_2	E (GPa)	σ_0 (MPa)
275	175	450	166.88	9.5
275	225	500	168.16	9.53
275	275	550	167.4	9.69
Average (X_{ave})			167.48	9.57
Standard Deviation (△X)			0.53	0.08
Standard Deviation / Average (△X/ X_{ave})			0.31%	0.87%